

# Protomylonite evolution potentially revealed by the 3D depiction and fractal analysis of chemical data from a feldspar

Ewa Słaby · Andrzej Domonik · Michał Śmigielski · Katarzyna Majzner · Gediminas Motuza · Jens Götze · Klaus Simon · Izabela Moszumańska · Łukasz Kruszewski · Paweł Rydelek

Received: 5 August 2013 / Accepted: 5 March 2014 / Published online: 25 March 2014  
© The Author(s) 2014. This article is published with open access at Springerlink.com

**Abstract** An alkali feldspar megacryst from a protomylonite has been studied using laser ablation-ICP-mass spectrometry combined with cathodoluminescence imaging, Raman spectroscopy, and electron probe microanalysis. The aim was to determine the original (magmatic) geochemical pattern of the crystal and the changes introduced by protomylonitization. Digital concentration-distribution models, derivative gradient models, and fractal statistics, e.g., Hurst-exponent values are used in a novel way to reveal subtle changes in the trace-element composition of the feldspar. Formation of the crystal is reflected in a slightly chaotic trace-element (Ba, Sr, and Rb) distribution pattern that is more or less characterized by continuous development from a fairly homogeneous environment. Derivative gradient models demonstrate a microdomain pattern. Fractal

statistics show that element behavior was changeable, with Ba and Sr always more persistent (continuing) and Rb always less persistent, with the latter showing a tendency to migrate. The variations in the Hurst exponent are, however, too large to be explained by magmatic differentiation alone. The observed element behavior may be explained by structural changes revealed by Raman spectroscopy and CL. In high-strain domains, T–O–T modes become stronger for Si–O–Al than Al–O–Al linkages. Increasing amounts of Al–O<sup>−</sup>–Al defects are demonstrated by cathodoluminescence. Both may result from small-distance diffusion creep, making the crystal geochemical pattern slightly patchy. In turn, the marginal part of the megacryst has a mosaic of randomly orientated, newly crystallized K-feldspars. The re-growth is confirmed by trace-element distribution patterns and fractal statistics which identify an abrupt change in the transformation environment. The novel set of tools used in this study reveals a complicated history of megacryst formation and transformation that otherwise would be difficult to unravel and decipher.

Communicated by J. Hoefs.

**Electronic supplementary material** The online version of this article (doi:10.1007/s00410-014-0995-5) contains supplementary material, which is available to authorized users.

E. Słaby (✉) · I. Moszumańska · Ł. Kruszewski  
Institute of Geological Sciences, Research Centre Warsaw, PAS,  
Twarda 51/55, 00-818 Warsaw, Poland  
e-mail: e.slaby@twarda.pan.pl

A. Domonik  
Institute of Hydrogeology and Engineering Geology, University  
of Warsaw, Żwirki i Wigury 93, 02-089 Warsaw, Poland

M. Śmigielski  
Department of Geology, Pope John Paul II State School of  
Higher Education in Biała Podlaska, Sidorska 95/97,  
21-500 Biała Podlaska, Poland

K. Majzner  
Raman Imaging Group, Faculty of Chemistry, Jagiellonian  
University, Ingardena 3, 30-060 Kraków, Poland

G. Motuza  
Department of Geology and Mineralogy, Vilnius University,  
Čiurlionio 21, Vilnius, Lithuania

J. Götze  
Institute of Mineralogy, TU Bergakademie Freiberg,  
Brennhausgasse 14, 09596 Freiberg, Germany

K. Simon  
Department of Geochemistry, GZG of Georg-August-University,  
Goldschmidtstrasse 1, 37077 Göttingen, Germany

P. Rydelek  
Department of Environmental Protection and Natural Resources,  
University of Warsaw, Żwirki i Wigury 93, 02-089 Warsaw,  
Poland

**Keywords** Alkali feldspar megacryst · Geochemistry · Raman spectroscopy · Fractal statistics · 3D depiction · Protomylonite

## Introduction

The imprint of a variety of petrogenetic processes is typically recorded in the composition and structure of mylonitized granitoids. Such rocks formed during a multistage process will reflect the interaction of superimposed events for which any precise definition and separation of overlapping effects is difficult to obtain. In such environments, the complex growth/re-growth history of a single mineral may reveal the entire sequence of rock-forming processes. To demonstrate such a history is the purpose of this paper.

Alkali feldspar is frequently used to give insight into complex magmatic and metamorphic processes (e.g., Vernon 1986, 2004; Knesel et al. 1999; Perini et al. 2003; Ginibre et al. 2004, 2007; Zellmer and Clavero 2006; Słaby et al. 2007a, b, 2008; Ishii et al. 2007; Menegon et al. 2008; Vernon and Paterson 2008). The composition of a megacryst, in recording many local events during magma evolution, can be expected to give detailed information about changes in its environment throughout the duration of its growth. Though sensitive to even subtle geochemical changes during crystallization, megacrysts are deemed to be relatively less sensitive to physical and compositional modifications in a metamorphic environment. They are more resistant to physical/structural deformation than other granitic phases such as quartz or mica which easily undergo grain reduction (Vernon et al. 1983; Vernon and Flood 1988; Vernon 2004). During deformation, however, the marginal parts of feldspars can recrystallize/neocrystallize, thus contributing to rock weakening. Reactions involving replacement of K-feldspar by myrmekite (Vernon et al. 1983; Simpson and Wintsch 1989; Tsurumi et al. 2003) are especially notable for producing fine-grained aggregates to be later transformed into foliae, contributing to rock deformation.

The transformation of K-feldspar into fine-grained assemblages is interpreted to be due to dissolution–precipitation creep proceeding along some preferred crystallographic axes (Ishii et al. 2007; Menegon et al. 2008). Dislocation creep or glide is rarely observed (Menegon et al. 2008). Svahnberg and Piazzolo (2013) noted the feedback between physical and chemical processes during feldspar deformation and recrystallization. Fluid commonly involved in these processes can easily infiltrate crystals, causing chemical re-equilibration. In plagioclases investigated by Svahnberg and Piazzolo (2013), asymmetrically zoned grains within high-stress areas were interpreted as related to dissolution–precipitation creep enhanced by

fluid–crystal interaction. Casini et al. (2009) pointed to a switch from dislocation to diffusional creep during recrystallization in the presence of water-rich fluid, a process which can proceed even at low temperatures. In wet facies, during metamorphism, as the fluid phase contains at least two volatile species, H<sub>2</sub>O and CO<sub>2</sub> (Bucher and Grapes 2011), a similar effect can probably be expected in the case of a CO<sub>2</sub>-rich fluid (Carroll and Knauss 2005). Electron backscatter diffraction (EBSD) is the most commonly used method to ascertain how feldspar is deformed (Schulmann et al. 1996; Ishii et al. 2007; Menegon et al. 2008; Svahnberg and Piazzolo 2013), and such studies are enhanced by the correlation of structural deformation with compositional changes in terms of major elements or focuses only on the physical impact on crystal structure.

This study tests new methods for (a) processing geochemical data and (b) recognizing structural changes in a K-feldspar megacryst from a mylonitized charnockitoid from the Lithuanian Kuršiai pluton. The results are applied to deciphering a complex evolutionary path involving a primary, magmatic geochemical pattern overprinted by mylonitization. In correlating the complexity of the trace-element distribution in a crystal with structural deformation, innovative tools are applied, namely, statistical analysis and depiction of trace-element distribution using digital concentration-distribution models (DC-DMs) and derivative models combined with fractal statistics. These tools potentially enable the identification and description of changes that occur during feldspar crystallization/recrystallization (Słaby et al. 2011, 2012). They may also allow the determination of the process dynamics in terms of element behavior and diffusion, and correlation with subtle structural changes.

## Geological setting

### Outline of basement structure

The Svecofennian orogeny (1.92–1.79 Ga; Lahtinen et al. 2008) produced widespread charnockitic magmatism in Western Lithuania. The Precambrian crystalline basement of Lithuania comprises of two principal domains, namely, the West Lithuanian Granulite Domain (WLGD) and the East Lithuanian Domain (ELD) that differ in structure, composition, and time of formation (Fig. 1). The crust of the WLGD is relatively thin (40–45 km), whereas that of adjacent domains exceeds 50–55 km. A remarkable feature of the WLGD is its thick (~30 km) upper crust and notably thin (~10 km) lower crust. A presumption that the WLGD formed during the accretion of volcanic island arcs toward the N-NE is based on the general manner of Svecofennian continental crust formation throughout the

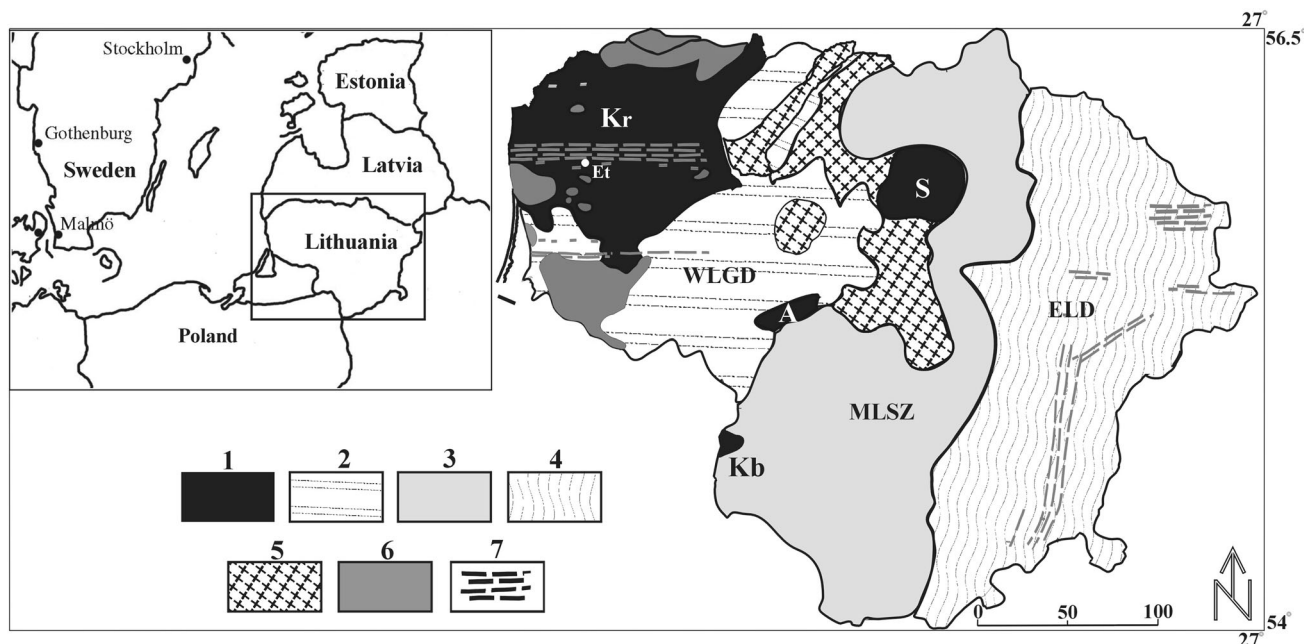


**Fig. 1** Sketch map of the crystalline basement in Lithuania [based on the geological map published in Motuza et al. (2008)]. Legend: 1—charnockitic plutons: *K* Kuršiai, *S* Sidabravas, *A* Ariogala, *Kb* Kybartai; 2—migmatized metasedimentary rocks of the West Lithuanian Granulite Domain (WLGD); 3—metavolcanic rocks of

the Mid-Lithuanian Suture Zone (MLSZ); 4—migmatized supracrustal rocks of the East Lithuanian Domain (ELD); 5—granitic intrusions coeval with the Kutršiai suite; 6—Mesoproterozoic cratonic granitic plutons; 7—fault rocks along main shear zones. Et—location of Eitučiai borehole

region (Nironen 1997; Bogdanova et al. 2006; Motuza 2005; Lahtinen et al. 2008).

The WLGD and the ELD are separated by the Mid-Lithuanian Suture zone (MLSZ) which is regarded as a collision zone (Fig. 1). Andesitic-dacitic metavolcanic rocks along the eastern margin of the WLGD suggest subduction of the ELD plate beneath the WLGD plate and its accretion toward the NW (Motuza 2005).

Intrusive rocks characterizing a large area of the crystalline basement are hosted by highly migmatized, granulitic supracrustal rocks, namely, garnet- and sillimanite-bearing metapelites, pyroxene-bearing calcium-rich gneisses, and biotite gneisses that pass into quartzite (Fig. 1). The supracrustal rocks are interpreted to have been clastic sediments (graywackes and feldspathic sandstones deposited in a collisional environment) intercalated with pyroclastics (Motuza and Staškus 2009). The almost complete absence of mafic metavolcanics is remarkable.

Charnockitic magmatism characterizes a few plutons in the WLGD (Fig. 1). Among them, the Kuršiai batholith is one of the largest in the western part of the East European Craton. Its age (zircon U–Pb) varies in the range 1.846–1.815 Ga (Claesson et al. 2001; Motuza et al. 2008), and it is coeval with other granitic plutons (1.836–1.844 Ga). Some younger (1.5–1.46 Ga) plutons also occur in the basement (Skridlaitė et al. 2007, 2008,

2010). With rare minor exceptions, gabbroic-dibasic mafic intrusive rocks are absent.

#### Mylonitized charnockitic rocks of the Kuršiai pluton

Charnockitic rocks are the most abundant rocks in the Kuršiai pluton (Fig. 1; Motuza et al. 2008). They are medium- (1–5 mm) to coarse-grained (5–10 mm) and commonly porphyritic with euhedral K-feldspar (<3 cm) and subhedral plagioclase phenocrysts. The typical mineral paragenesis comprises hypersthene (~20 vol%), clinopyroxene, biotite, K-feldspar, plagioclase (An<sub>35-45</sub>–An<sub>55</sub>), quartz (including myrmekite), and, commonly, garnet (<20 vol%). Accessory minerals are magnetite, hercynite, monazite, apatite, and zircon. Amphibole substitutes for pyroxene in some instances. The rocks are massive and homogeneous, but commonly also gneissic. A gneissic fabric, due to mylonitization, is strongly developed in some shear zones.

For our study, an alkali feldspar megacryst was sampled from the Eitučiai-1 drill core (Fig. 1) taken from a borehole located in the Telšiai shear zone. The rocks in that location show varying degrees of mylonitization that occurred under conditions transitional from granulite to amphibolite facies. The PT values estimated by Skridlaitė and Smilgienė (2004) are  $P = 6\text{--}7.5$  kbar and  $T = 600\text{--}680$  °C and, by Vėjeljytė (2011),  $P = 4\text{--}6$  kbar and  $T = 680\text{--}750$  °C.



The host sample was taken from the 1,992 to 2,034 m interval of the core. The rock is a coarse-grained porphyritic garnet-biotite opdalite with large (2–3 cm) pink alkali feldspar megacrysts (Fig. 2a). The texture varies from porphyritic to mylonitic (Fig. 2b–f). The alkali feldspar megacrysts are euhedral and contain many inclusions of plagioclase and accessory minerals. The plagioclase inclusions are typically altered, with

myrmekite in their marginal parts (Figs. 2b, 8e). In addition, some large (3–7 mm) plagioclase crystals host small alkali feldspar inclusions (Fig. 2c, f). Plagioclase either shows mechanical twinning or is untwinned and slightly patchy (Figs. 2c, f, 8f). Intergranular, very fine-grained bands in the rock are developed from tiny fragments of quartz, feldspar, and biotite. Quartz commonly forms ribbons or lenses.

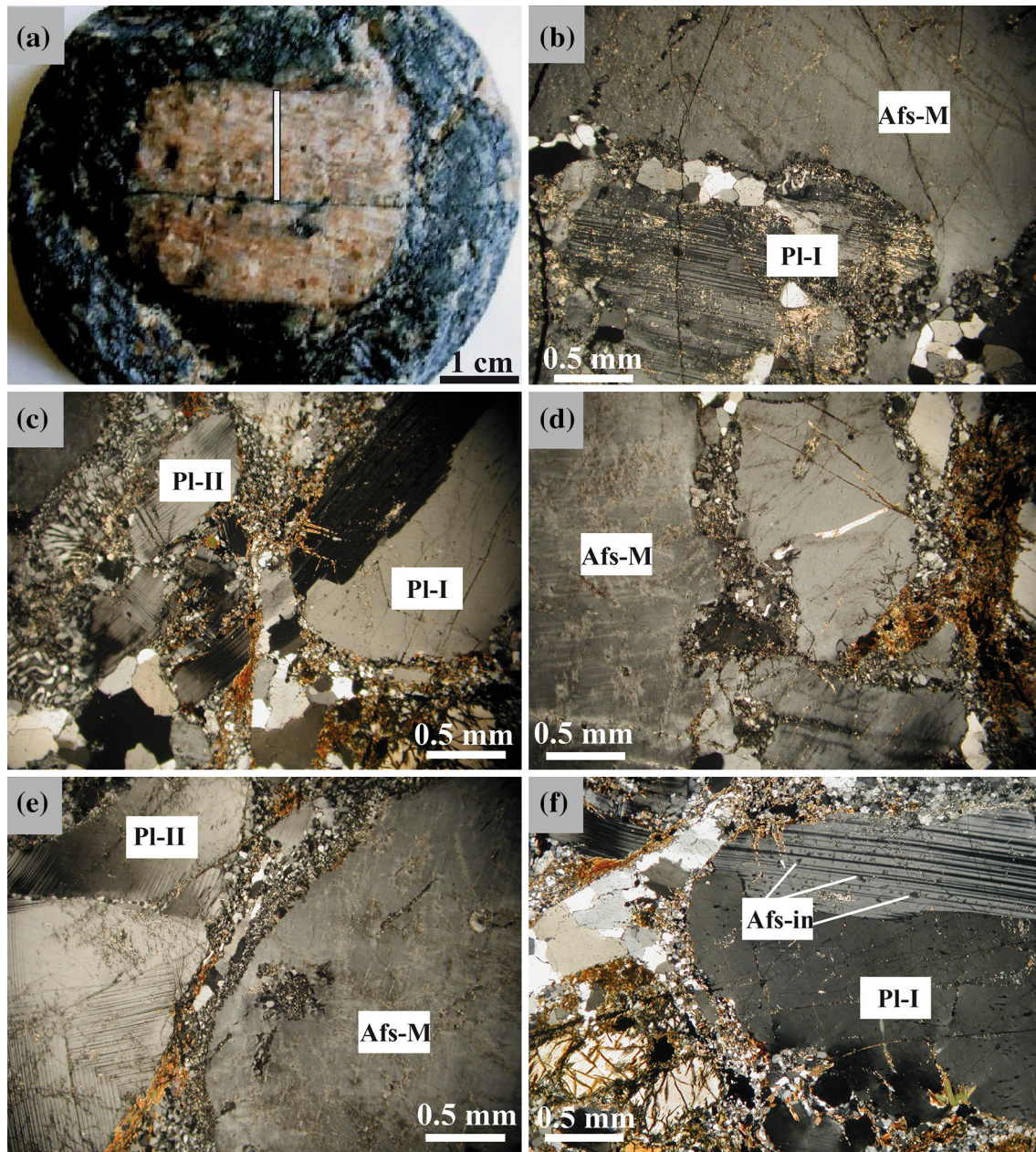


**Fig. 2** Porphyritic opdalite from the Eitučiai-1 drill core. **a** Drill core with the alkali feldspar investigated. The *line* shows the LA-ICP-MS transect; **b** alkali feldspar megacryst with altered plagioclase; **c** fresh plagioclases embedded in quartz-biotite matrix; myrmekite zones between alkali feldspar megacryst and plagioclase; **d**, **e** marginal parts

of alkali feldspar megacryst with small plagioclase inclusions surrounded by mylonitic matrix; **f** fresh plagioclase with small alkali feldspar inclusions. *Afs-M* alkali feldspar megacryst, *Afs-in* alkali feldspar inclusions, *Pl-I* plagioclases of first generation, *Pl-II* plagioclases of second generation (see text for further explanation)

## Methods

### Laser ablation-ICP-mass spectrometry

Laser ablation-ICP-mass spectrometry (LA-ICP-MS) was carried out at the Geochemisches Institut, Göttingen University, using a FISIONS VG PQ STE instrument with a VG UV Microprobe laser system (266 nm). The megacryst was analyzed for  $^{23}\text{Na}$ ,  $^{27}\text{Al}$ ,  $^{29}\text{Si}$ ,  $^{39}\text{K}$ ,  $^{43}\text{Ca}$ ,  $^{49}\text{Ti}$ ,  $^{55}\text{Mn}$ ,  $^{57}\text{Fe}$ ,  $^{85}\text{Rb}$ ,  $^{88}\text{Sr}$ ,  $^{133}\text{Cs}$ ,  $^{137}\text{Ba}$ ,  $^{139}\text{La}$ ,  $^{140}\text{Ce}$ ,  $^{141}\text{Pr}$ ,  $^{143}\text{Nd}$ ,  $^{147}\text{Sm}$ ,  $^{151}\text{Eu}$ ,  $^{157}\text{Gd}$ ,  $^{159}\text{Tb}$ ,  $^{163}\text{Dy}$ ,  $^{165}\text{Ho}$ ,  $^{166}\text{Er}$ ,  $^{169}\text{Tm}$ ,  $^{172}\text{Yb}$ ,  $^{175}\text{Lu}$ , and  $^{208}\text{Pb}$  at points every 270  $\mu\text{m}$  along transects from rim to core. Elemental concentrations were calculated using NBS610 for calibration and  $^{29}\text{Si}$  as an internal standard. Major-element oxides (concentrations compared with EMPA results) were normalized to sum to 100 %. Internal reproducibility, indicated by standard deviations, in most cases is better than 2 % RSD for both concentrations and ratios. Of all the analyzed trace elements, only three (Ba, Sr, Rb) provided concentrations suitable for detailed petrogenetic analysis. The concentrations shown by the remainder were deemed too low for reliable modeling. For the Ba, Sr, and Rb used for detailed petrogenetic analysis, standard deviation RSD was 2 %. Statistical comparison of the element concentrations was made several times using different levels of  $1\sigma$  uncertainty from 0 to 10 % of the measured values and the results compared. At the same time, the ratios of Ba/Sr/Rb were estimated with an error of less than 3 %, leaving the very high probability that any over- or underestimation, if such occurred, affects all elements in the same manner.

### Electron probe microanalysis

The K-feldspar megacryst was profiled by electron microprobe (EMPA) point analyses in 5- $\mu\text{m}$  steps. Major elements (Na, Al, Si, K, Ca) and some trace elements (Ba, Mg, Fe) were determined. Chemical analyses of the megacryst were performed at the Laboratoire Magmas et Volcans, Clermont-Ferrand) with a Cameca SX-100 (accelerating voltage 15 kV; two conditions of beam current). Alkalies, Ca, Si, and Al, were analyzed at 15 nA. Trace elements were analyzed at 50 nA. Counting times were 30 s for Fe and Mg, 60 s for Al and Si, and 10 s for Ca. The EMPA transect was done to get reliable data on the major-element composition of the alkali feldspar, to test the accuracy of the LA-ICP-MS major- and trace-element (Ba) data. Representative detection limits ( $3\sigma$ ) for minor- and trace elements were 220 ppm for Ba, 200 ppm for Fe, and 40 ppm for Mg. Thin section Ba, Na, K, and Ca maps were made using an accelerating voltage of 15 kV, a beam current of 100 nA, steps of 20  $\mu\text{m}$ , a dwell time of 40 ms, and a beam diameter of 10  $\mu\text{m}$ . Applying the Monte Carlo

simulation, the interaction depth of the electron beam with the sample was  $<5\ \mu\text{m}$ . Figure 1 (electronic supplement) shows data from both microprobe- and LA-ICP-MS traverses to test the accuracy of the LA-ICP-MS trace-element (Ba) data.

### Digital models

LA-ICP-MS data were used to create DC-DMs of Ba, Sr, and Rb contents. The 45 LA-ICP-MS spots were located along a 12-mm long traverse (X axis; 1st dimension). The distance between the center points of spots was  $\sim 270\ \mu\text{m}$ . Each laser ablation pulse lasted 20 ms was  $\sim 100\ \mu\text{m}$  in diameter and gave data from a 5- $\mu\text{m}$  thick layer of feldspar. This measurement, repeated every 0.943 s, provides a complete chemical analysis. The next pulse, ablating a deeper part of feldspar, does not interfere with that before, as the aerosol is removed by the carrier gas within 1 s. About 100 impulses were used within one spot; the number of laser impulses, and the depth reflects the duration of each LA-ICP-MS analysis (Y axis; 2nd dimension). Observed variations in ppm contents of the elements with depth are related to the Z axes (3rd dimension). As the result, three separate grids (DC-DMs) of Ba, Sr, and Rb contents were created. All models have the same spatial resolution and single grid consisting of more than 4,000 single measurements. The reliability of the model is discussed in Słaby et al. (2008, 2011) and Śmigielski et al. (2012). Before depiction, models were geostatistically analyzed using variograms in order to provide preliminary estimates of degree of spatial dependence. Variogram parameters such as the nugget effect, sill, and range were estimated. The spatial anisotropies of the whole models and of their different parts were calculated (Matheron 1963; Gringarten and Deutsch 2001).

For qualitative analysis, the DC-DMs were depicted using Surfer 8.0 (Golden Software); isoline maps and 3D models were merged with shaded relief images (Yoeli 1965). The Surfer 8.0 “terrain slope” and “terrain aspect” functions were used to calculate values of the maximum gradient and the direction of maximum gradient, respectively. The maximum gradient was depicted as the angle of the slope of the change in concentration with values close to  $0^\circ$  representing a flat surface (almost no change in concentration) and values close to  $90^\circ$  abrupt changes in concentration. Additionally, in order to compare the dynamics of concentration change between elements, gradients were normalized using average ppm concentrations, calculated separately along the X and Y axes of the model, and then normalized to Ba dynamics. The direction of the maximum gradient (direction of the maximum rate of concentration change) was preliminarily calculated as an azimuth and then simplified to four



sectors. Two different sets of colors were applied to the sectors in order not to bias interpretation. The data were not interpolated, but depictions were preceded by a spline smoothing procedure without any re-calculation of the model. The procedure did not affect the distribution or the value of the data, but gives enhanced images at higher resolutions. Both true X–Y scale and Y exaggerated models were prepared and analyzed. Exaggeration along laser spots allows visual compensation for differences in data-collection resolution and was taken into account during interpretation. The Z dimension (ppm) in the DC-DM has no spatial relation to X and Y that represent the spatial position of the measurement. The Z scale was arbitrarily chosen to further improve the quality of the data depiction, and to best display the spatial distribution of an element's concentration. Different directions of lighting were used in analyzing various aspects of the morphology of the surface (Cooper 2003).

Following procedures described in Słaby et al. (2011) and Śmigielski et al. (2012), the Ba, Sr, and Rb DC-DMs were compared using cut-off level and gradient models. These qualitative procedures allow the levels of compatibility (accordance) between element distributions in the crystal to be estimated. The first procedure involves comparison of the relative concentration values for any two elements determined against their average concentration. The second method consists of discriminating (with application of the first derivative) between those areas of two different DC-DM where the concentrations of an element increase or decrease simultaneously. In both cases, the concept of “probability of accordance” was used in order to include uncertainty produced by LA-ICP-MS (Słaby et al. 2011).

### Fractal analysis

A fractal-based method—rescaled range analysis (R/S)—was used to detect the presence or absence of a trend in the time series (nonstationary signals, e.g., geochemical series of data) by finding the Hurst exponent (Mandelbrot and Van Ness 1968). The Hurst exponent gives a measure of the smoothness of a fractal object where  $H$  varies between 0 and 1 and helps to distinguish between random and nonrandom data patterns. The fractal dimension  $D$  was derived from the Hurst exponent  $H$  by the relation  $D = 2 - H$ . In the present work,  $H$  is calculated using the Hurst rescaled range analysis method (R/S) as improved by Peters (1994). For a given set of data series  $x_1, x_2, \dots, x_n$  (selected LA-ICP-MS profiles), for  $n$  periods (number of sectors) and a sample mean  $\bar{x}_n$ , the classical rescaled range formula is expressed as follows:

$$R/S = \frac{1}{S} \left[ \max_{1 < k < n} \sum_{j=1}^k (x_j - \bar{x}_n) - \min_{1 < k < n} \sum_{j=1}^k (x_j - \bar{x}_n) \right]$$

where  $S$  is the standard deviation. The relationship between  $R/S$  and  $H$  can be expressed as  $R/S = an^H$  (where  $n$  is the number of data points in a data series and  $a$  is a constant associated with standard deviation). The Hurst exponent can be estimated using the regression  $\text{Log}(R/S) = \text{Log}(a) + H(\text{Log}(n))$  and by plotting it where  $Y = \text{log } R/S$  and  $X = \text{log } n$  and the exponent  $H$  is the slope of the regression line (Domonik et al. 2010).

### Raman mapping

Raman mapping was done for some areas along the transect analyzed by LA-ICP-MS, using a Confocal Raman Imaging system (Witec alpha 300) and a Nikon 20× air objective (SPlan Fluor Nikon; NA = 0.45). Scattered light was directed to the spectrometer using a 50-μm core diameter multimode fiber which also acted as the pinhole for confocal detection. The Witec Raman spectrometer equipped with a back-illuminated CCD (Newton EMCCD DU970-BV) camera and a 600 grooves/mm grating (BLZ = 500 nm) has a spectral resolution of around 3 cm<sup>-1</sup>; a Nd:YAG dye laser has a maximum power at source of ca 40 mW at 532 nm. Raman spectroscopic maps resulting from imaging at 532 nm of the excitation wavelength and a laser power of ca 30 mW at the sample were obtained by collecting spectra with a 0.4 s exposure time and moving the sample in increments of 2 μm (120 × 120 μm<sup>2</sup>; 3,600 points). Total exposure time per map was ~24 min. Data acquisition was controlled by the Witec alpha 300 software package.

The Witec Project Plus software used for preliminary data analysis enables investigation of the spatial distribution of chemical components in the measured feldspar area by integrating the selected bands and doing k-means cluster analysis. All spectra were baseline corrected using a polynomial of degree 3 or 6 and the routine procedure for cosmic-ray removal was applied.

The first step in data evaluation was the normalization of spectra in the 80–1,500 cm<sup>-1</sup> region using the Manhattan normalization mode. In this mode, two identical spectra with different intensities will be comparable. A variant of cluster analysis (k-means Cluster Analysis—KMC) of the recorded spectra was performed by using a Manhattan algorithm as a distance measurement and a linkage method according to the city block algorithm. Mean spectra of the classes obtained were calculated by averaging original spectra from all pixels within a class.

Further analysis of the spectral data was carried out using OPUS 7.0 software. This program allows spectral preprocessing (e.g., normalization, smoothing, baseline correction, second derivative, integration of bands) and chemometric data analysis. Mean Raman spectra were normalized to the band at  $\sim 515\text{ cm}^{-1}$  ( $493\text{--}546\text{ cm}^{-1}$  range) using the vector normalization method, and the integrated areas of bands at 266, 282, 455, 480, and  $515\text{ cm}^{-1}$  were calculated. As the next step, band-area ratios for selected Raman bands, i.e.,  $I_{266}/I_{282}$ ,  $I_{480}/I_{455}$ ,  $I_{515}/I_{455}$ ,  $I_{515}/I_{480}$ , were determined for each spectrum.

#### Cathodoluminescence study

CL microscopy and spectral CL measurements were used to document internal textures within the K-feldspar phenocrysts. The CL measurements were taken on carbon-coated, polished thin sections using a hot cathode CL microscope (HC1-LM; Neuser et al. 1995) operated at 14 kV accelerating voltage and a current density of ca  $10\text{ }\mu\text{A}/\text{mm}^2$ . Luminescence images were captured online with a Peltier-cooled digital video camera (KAPPA 961-1138 CF 20 DXC). CL spectra in the wavelength range 380–1,000 nm were recorded with an Acton Research SP-2356 digital triple-grating spectrograph with a Princeton Spec-10 CCD detector attached to the CL microscope by a silica-glass fiber guide. CL spectra were measured with wavelength calibration by Hg-halogen lamp (spot width  $30\text{ }\mu\text{m}$  and measuring time 2 s).

#### Megacryst study: results

The megacryst ( $2.5\text{ cm} \times 4\text{ cm}$ ) studied was separated from the protomylonite and cut so that its cross section crossed the central core of the crystal. Some random cross sections of other megacrysts were examined in order to recognize crystal growth or re-growth textures. The megacrysts were not entirely homogeneous (Table 1; compare Na and K contents). Even if there was no clear development of perthite, wavy, undulose extinction provided evidence that exsolution was in progress. No zonal growth development was recognized by imaging with the petrographic microscope, backscattered electrons, or cathodoluminescence. All imaging methods showed almost uniform, only slightly maculate feldspars. The crystals were variably cracked. The trace-element data for the chosen megacryst were acquired using LA-ICP-MS. Initially, the whole crystal was profiled by microprobe point analysis to get preliminary information on compositional variation along the whole transect, with special emphasis on Ba content. The microprobe traverse (Figure 1, electronic supplement) showed that the core and middle parts

of the megacryst display a compositional plateau of almost constant Ba concentration that decreases toward the crystal margins. Thin section-sized maps of Ba, Na, K, and Ca X-ray intensities (not shown) demonstrate a lack of zoning in these elements. Marginal parts of the crystal reveal a slightly different composition (enriched in K, impoverished in Ba). Taking under consideration the preliminary data, only one half of the crystal was chosen for the LA-ICP-MS transect. Comparison of the EMPA and LA-ICP-MS data allowed the conclusion that the analytical transect and number of points sampled by LA-ICP-MS provided a reliable picture of the compositional variation in terms of trace elements.

Megacryst composition: DC-DMs (digital concentration-distribution models), derivative models, element distribution accordance, fractal statistics

The feldspar composition was determined along a single transect in evenly spaced steps giving 45 LA-ICP-MS spots (Fig. 2a)—from spot 1 in the crystal margin to spot 45 on the core. Twenty-seven elements were analyzed. Though most were not suitable for making 3D depiction models, all were necessary for reliable identification of the phase composition at each spot. Some spots show alkali feldspar compositions obscured by fine accessory mineral inclusions, and some are dominated by accessory minerals. The data are summarized in Table 1. Three elements of contrasting geochemical affinity (Ba, Sr, Rb) were chosen for the reconstruction of the megacryst formation/transformation history. Ba and Sr behave compatibly. Depending on environment composition, Rb can show compatible- or incompatible behavior (Nash and Crecraft 1985; Mahood and Stimac 1990; Ewart and Griffin 1994; Icenhower and London 1996). Their diffusion rates in silicates are different. Ba diffusion in an alkali feldspar crystal is slower than that of Sr by about two orders of magnitude (Cherniak 1996, 2002) and the activation energy of Rb is higher than that of Sr (Giletti 1991).

The spatial distribution of these elements is presented as DC-DMs on Fig. 3. True-scale and exaggerated models of Ba, Sr, and Rb distribution depicted as contour maps and as 3D surfaces show that the geochemical pattern of the analyzed feldspar is perturbed by the presence of several inclusions (Figs. 3, 4; Table 1). The irregularities give the distributions a seemingly zoned pattern. The zones are continuous along the inclusion-rich spots or appear at some depth, and disappear. Major inclusions occur in spots 1–2, 6, 9, and 37–38, and minor inclusions at spots 21, 26, and 30 (Fig. 3; Table 1). In order to evaluate the true character of the geochemical pattern not influenced by inclusions, both qualitative and statistical analysis were performed not only for the whole data set (spots 1–45) but also separately

**Table 1** Composition of alkali feldspar megacryst—LA-ICP-MS data (in ppm; average for each spot)

Spot	Na	Mg	Mg	P	K	Ca	Ti	Fe	Ga	Rb	Sr	Y	Cs	Ba	La	Ce	Pr	Nd	Sm	Eu	Gd	Dy	Pb
1	3562	305	301	218	62069	749	86	819	4	118	79	1	1	1631	5	5	0	2	1	2	0	0	22
2	614	160	149	78	13363	539	64	503	2	49	18	0	0	465	2	2	0	1	0	0	0	0	12
3	8263	608	570	161	137916	1355	73	1458	8	274	146	1	1	3222	11	11	1	2	0	3	0	0	32
4	10434	799	761	176	176643	1475	73	2378	11	349	179	0	2	3983	10	8	0	1	0	3	0	0	43
5	10551	461	442	165	170481	1256	55	1340	10	328	184	0	2	3776	7	5	0	1	0	3	0	0	42
6	4043	77684	70920	229	166528	3154	35906	173359	39	858	49	13	16	2734	13	16	2	8	2	1	3	2	24
7	9776	8197	7812	196	171887	2013	3304	21278	14	417	208	5	4	4274	7	7	1	2	1	4	1	1	46
8	9239	409	376	157	186969	1193	194	1191	12	379	190	0	2	4414	6	5	0	0	0	3	0	0	49
9	40756	22205	20998	208	38413	23813	4796	46727	30	114	156	11	2	558	24	40	4	14	2	2	2	2	12
10	9650	2502	2406	171	162625	1581	266	6648	12	334	180	1	14	4230	6	5	0	1	0	3	0	0	38
11	9043	288	256	155	184340	1107	61	873	12	380	212	0	2	4918	6	4	0	0	0	4	0	0	45
12	9210	173	159	164	191853	953	60	775	13	417	233	1	3	5675	6	6	0	1	0	4	0	0	62
13	9642	375	359	270	186064	1032	51	761	11	374	209	3	2	5016	7	8	1	3	1	4	1	1	47
14	8959	264	266	284	189687	1318	47	522	11	369	219	3	2	5207	6	6	1	1	0	4	0	0	47
15	10257	100	90	284	190060	2673	45	329	11	393	217	4	2	5590	10	13	1	4	1	4	1	1	49
16	9061	87	87	273	196245	1153	50	297	11	389	223	2	2	5431	8	9	1	2	0	4	0	0	48
17	8507	66	56	278	193363	1422	55	355	11	391	210	4	2	5339	7	8	1	2	1	4	1	1	46
18	8624	653	628	263	192808	1487	55	2056	11	373	221	2	2	5232	6	7	1	2	0	4	0	0	48
19	9991	378	362	290	194539	1419	54	1254	11	392	218	3	2	5272	8	9	1	2	0	4	1	1	46
20	10390	28	28	313	189635	1346	55	255	11	393	216	4	2	5213	11	13	1	4	1	4	1	1	44
21	16284	1220	1170	232	157140	6731	50	2825	11	335	197	4	2	4468	13	16	1	4	1	3	1	1	39
22	11652	307	284	285	188048	2372	57	867	11	385	217	4	3	5234	8	9	1	2	1	4	0	1	47
23	9990	187	189	268	198628	1383	50	619	12	407	220	2	3	5507	12	12	1	3	0	4	0	0	49
24	10097	274	264	314	202034	1446	52	1027	13	411	217	4	3	5443	11	13	1	3	1	4	1	1	46
25	11204	42	40	312	200383	1567	55	229	12	407	217	3	3	5572	9	10	1	2	1	4	1	1	44
26	7629	8885	8845	278	173280	1383	46	19787	12	340	183	4	2	4494	11	14	1	5	1	3	1	1	43
27	9387	622	618	242	202954	1219	48	2166	12	410	227	8	3	5390	11	14	1	5	1	4	1	1	48
28	9346	399	397	296	226341	1226	52	977	12	435	235	1	3	5402	6	6	0	1	0	4	0	0	50
29	9636	424	433	241	226892	1147	60	1460	14	447	241	1	3	5473	8	7	0	1	0	4	0	0	53
30	14753	1112	1133	175	211553	1732	46	3683	13	411	199	1	2	4778	4	2	0	0	0	3	0	0	36
31	9688	243	261	289	243126	1427	53	884	13	461	255	3	3	5352	9	9	1	2	0	4	0	1	55
32	10908	52	56	340	245871	1872	61	328	13	463	244	5	3	5446	12	12	1	3	1	4	1	1	50
33	13490	226	237	205	231626	2187	57	1033	14	463	249	1	3	5029	12	13	1	3	0	4	0	0	72
34	9333	65	66	307	259491	1854	129	420	13	497	248	4	3	5263	12	13	1	3	1	4	1	1	53
35	11591	9	11	369	260522	2245	68	229	14	491	241	6	3	5334	12	13	1	4	1	4	1	1	54
36	11777	5	3	358	262831	1672	67	138	15	494	289	5	3	5565	10	11	1	3	1	4	1	1	64



Table 1 continued

Spot	Na	Mg	Mg	P	K	Ca	Ti	Fe	Ga	Rb	Sr	Y	Cs	Ba	La	Ce	Pr	Nd	Sm	Eu	Gd	Dy	Pb
37	16987	237	254	645	210079	11026	85	1409	14	399	216	2	2	3849	15	20	2	6	1	3	1	0	46
38	4366	79871	80730	288	204205	6572	96893	265206	72	1105	29	18	22	2655	14	17	2	9	2	1	3	3	20
39	8928	1329	1594	353	275993	1461	1425	6346	17	537	277	3	4	5476	7	6	0	1	0	4	0	1	53
40	9248	128	136	318	289678	1416	86	580	14	532	272	2	3	5288	5	3	0	0	0	4	0	0	60
41	10990	124	126	270	288604	1561	58	586	15	517	264	2	3	5165	6	4	0	1	0	4	0	0	61
42	11123	142	152	303	284122	2269	61	637	15	517	264	2	3	5243	9	9	1	2	0	4	0	0	60
43	11178	15	13	198	282218	1983	55	214	15	513	263	0	3	4991	8	6	0	1	0	4	0	0	58
44	7323	2133	2236	244	307372	1671	57	7544	17	532	285	1	4	5260	6	4	0	1	0	4	0	0	71
45	8871	247	258	188	297182	1470	50	1038	15	521	308	0	2	5062	8	5	0	0	0	5	0	0	70

Data from spots dominated by accessory minerals are underlined

for the middle part of the crystal where the influence of inclusions is minor (spots 11–36) and for a section of mostly pure feldspar (spots 11–20).

Geostatistical analysis shows a strong anisotropy in the spatial distribution of all three elements. Much longer variogram ranges for the Y direction of the models confirm that the general pattern is dominated by zones (Fig. 4). However, this is not true for the 11–36 and 11–20 sections, where the absence or near absence of major inclusions leads to the ellipse of anisotropy being elongated in a roughly perpendicular direction compared with the ellipse shape for the whole data set. Oscillatory zoning is not evident. This is also confirmed by the value of the nugget effect, which increases for “pure” feldspar, and is almost zero for the whole data set. An absence of a zone-like arrangement of Ba, Sr, and Rb in feldspar free of inclusions is indicated in Fig. 4.

The DC-DM models show that the Ba distribution is slightly patchy. The dots are chaotically dispersed, but the intensity of the patchiness differs for different crystal areas. Careful observation allows some areas of similar element behavior to be distinguished. The most homogeneous composition characterizes the core area between spots 45 and 30 (Fig. 3a). The heterogeneity in Ba distribution extends beyond spot 30 and is clearly visible up to spot 21 before decreasing again beyond spot 21. The intervals between spots 29–20 and 20–11 are taken to define the inner- and outer middle zones, respectively. The spots with inclusions (38–37, 30, 26, and 21) are markers separating areas showing subtle changes in element distribution. The marginal part of the depiction (spots 1–9) shows progressive depletion in Ba content. This pattern is, however, strongly disturbed by inclusions, in particular at spot 9 which involves a mixture of plagioclase and accessory phases.

As with Ba, the crystal core exhibits the greatest Sr enrichment (Fig. 3b), progressively diminishing outwards. The core also shows the most homogeneous Sr distribution (spots 45–39). Beyond spots 38–37, the distribution is more heterogeneous up to spot 30–25, beyond that Sr contents hardly change up to spot 9. The decline in Sr content is more marked than that of Ba and, as with Ba, the most marked decrease occurs between in the marginal zone.

Rb follows the Sr pattern. Only the core (spots 45–39) is relatively Rb-rich (Fig. 3b). With the exception of spot 38 containing Rb-rich inclusions, Rb contents decrease slowly outwards to spot 25. In the outer middle zone, Rb contents are almost constant before falling away progressively in the marginal part. Spots 6 and 7 with Rb-rich inclusions are the exception.

Some systematic changes characterize all the ablated spots. Rb decreases systematically with depth in 39 of the

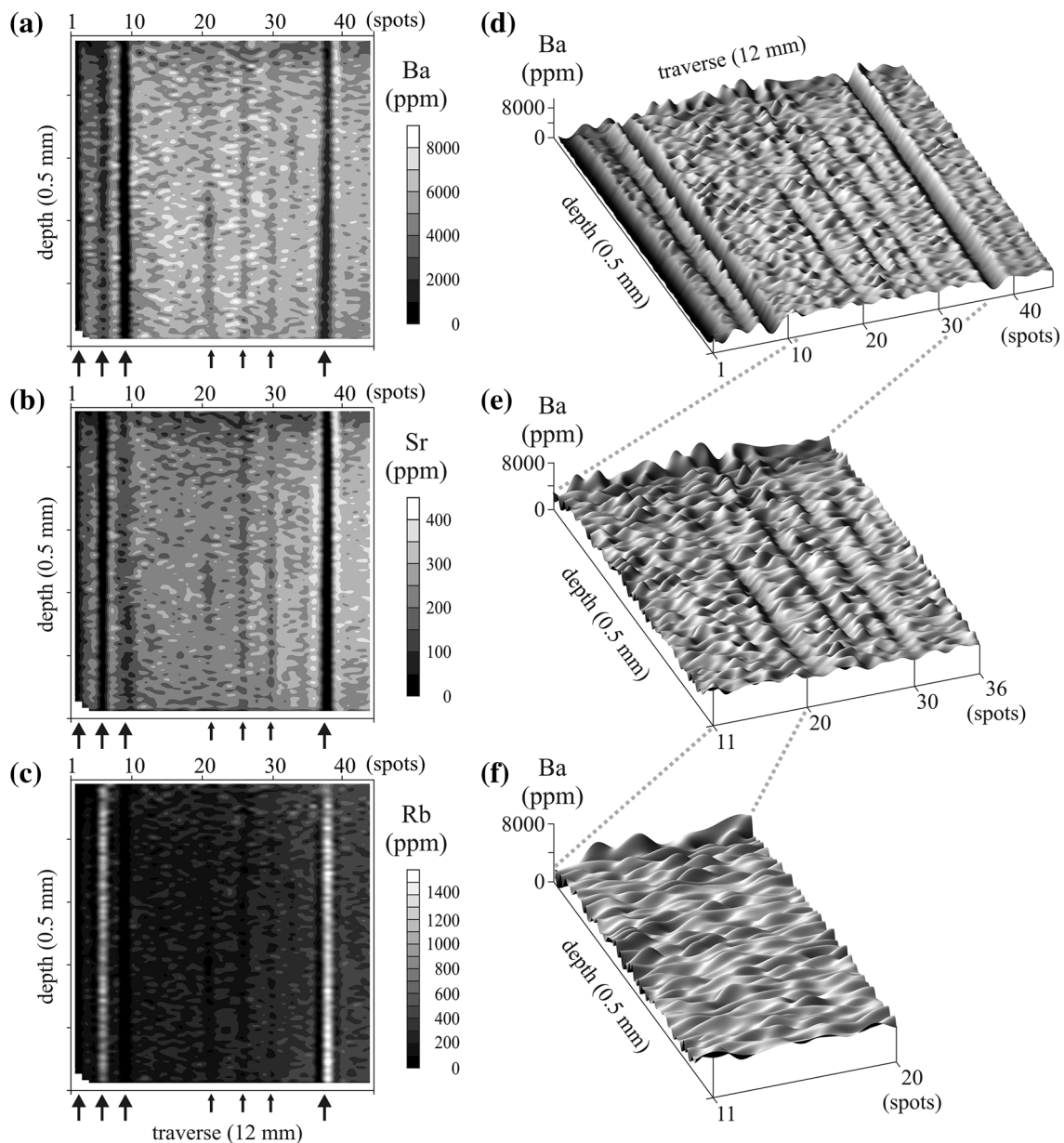


**Fig. 3** Depiction of DC-DM for of Ba, Sr, and Rb (a–c) along the whole investigated transect (*left side* crystal margin, *right side* crystal core). The distribution pattern is very regular for all of the elements. Divergences to the *left* (spots 6–7 and 9–10) and to the *right* (spots 37–38–39) are due to mineral inclusions (marked with *arrows*). A weak influence by accessory minerals is also seen in spots 21, 26, 30

(*small arrows*). 3D-shaded relief models of Ba distribution (d–f) for different parts of analyzed profile: **d** whole data set (spots 1–45), **e** excluding major inclusions (spots 11–36), **f** feldspar without inclusions (spots 11–20). Models show influence of the inclusions on the general geochemical pattern and lack of zoning in the inclusion-free feldspar. Instead, a more patchy distribution is visible

45 spots and Ba and Sr increase likewise in 28 and 30 spots, respectively. The interelement relationship is not linear (not shown).

The LA-ICP-MS data allow for a further qualitative analysis of the relationship between different elements. The relationships between compatible- (Ba, Sr, Eu) and incompatible elements (Cs, Y, Ce), and between three elements (Rb, Pb, Ga) which can exhibit both compatible

and incompatible characteristics (Nash and Crecraft 1985; Mahood and Stimac 1990; Ewart and Griffin 1994; Icenhower and London 1996), are shown on Fig. 5. In some cases, a single linear trend appears (e.g., Eu vs Sr, Rb vs Sr), in others, the data show considerable scatter. The core of the crystal, the adjacent middle zone, and the marginal zone are distinguished. All the plots show similar trends. Data for all areas partly overlap.

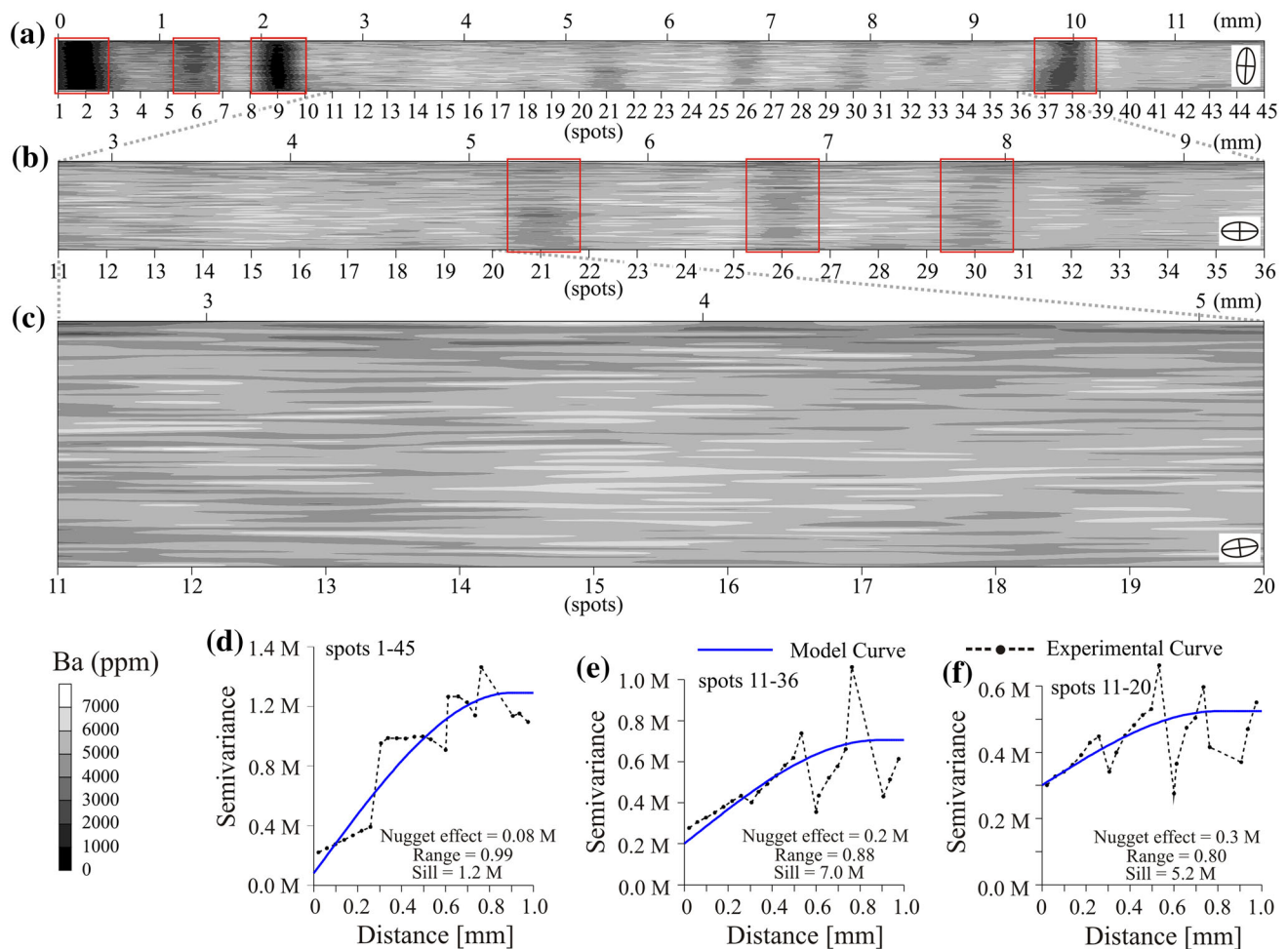


**Fig. 4** DC-DM of Ba as contour maps without exaggeration **a** for the whole analyzed portion of the crystal including major inclusions **b** for spots 11–36 and **c** for spots 11–20. Red rectangles mark inclusions. Ellipses of anisotropy of the spatial correlation with the data distribution are shown. Please note lack of zonation in the feldspar

and its patchy texture. True shape of the patches is difficult to recognize due to differences in the resolution of data collection in X and Y directions. Variograms of spatial data distribution for Ba **d** for the whole data set, **e** for spots 11–36, **f** for the spots 11–20. Range, sill, and nugget effect are given

In summary, the DC-DMs models, their depictions, and the qualitative analysis of the relationships between elements on the binary diagrams (Figs. 3, 4, 5) suggest some differences in the behavior of the various elements. The differences cannot be estimated by the reference to DC-DMs only. In order to establish the degree of persistency (continuity) in the behavior of the elements, the Hurst exponent was calculated for the data set from each spot (Table 1, electronic supplement). The Hurst exponent ( $H$ ) is a self-similarity parameter (Mandelbrot and Van Ness 1968). Its value, which ranges from 0 to 1, reflects the long-range dependence of element behavior during a process.  $H = 0.5$  indicates a random distribution indistinguishable from noise. For values higher or lower than 0.5, the system displays nonlinear dynamics, though with different levels of persistency.  $H < 0.5$  reflects antipersistent

(more chaotic) behavior and  $H > 0.5$  increasing persistence (less chaotic).

In the processed data, preceding values constantly affect succeeding values in the entire temporal series. In the language of probability, for  $H > 0.5$ , a trend generated by a process in the past will most likely be continued in the future. The system exhibits a low degree of deterministic chaos. In contrast,  $H < 0.5$  indicates a process characterized by frequent and sudden reversals. Low  $H$  values predict with a high probability that an earlier tendency in a trend will induce change in the future. Thus, the system can be described as having a high degree of deterministic chaos.

Calculated  $H$  values for Ba, Sr, and Rb are generally high; average values for all spots are 0.83, 0.84, and 0.76, respectively (Table 1, electronic supplement). Very



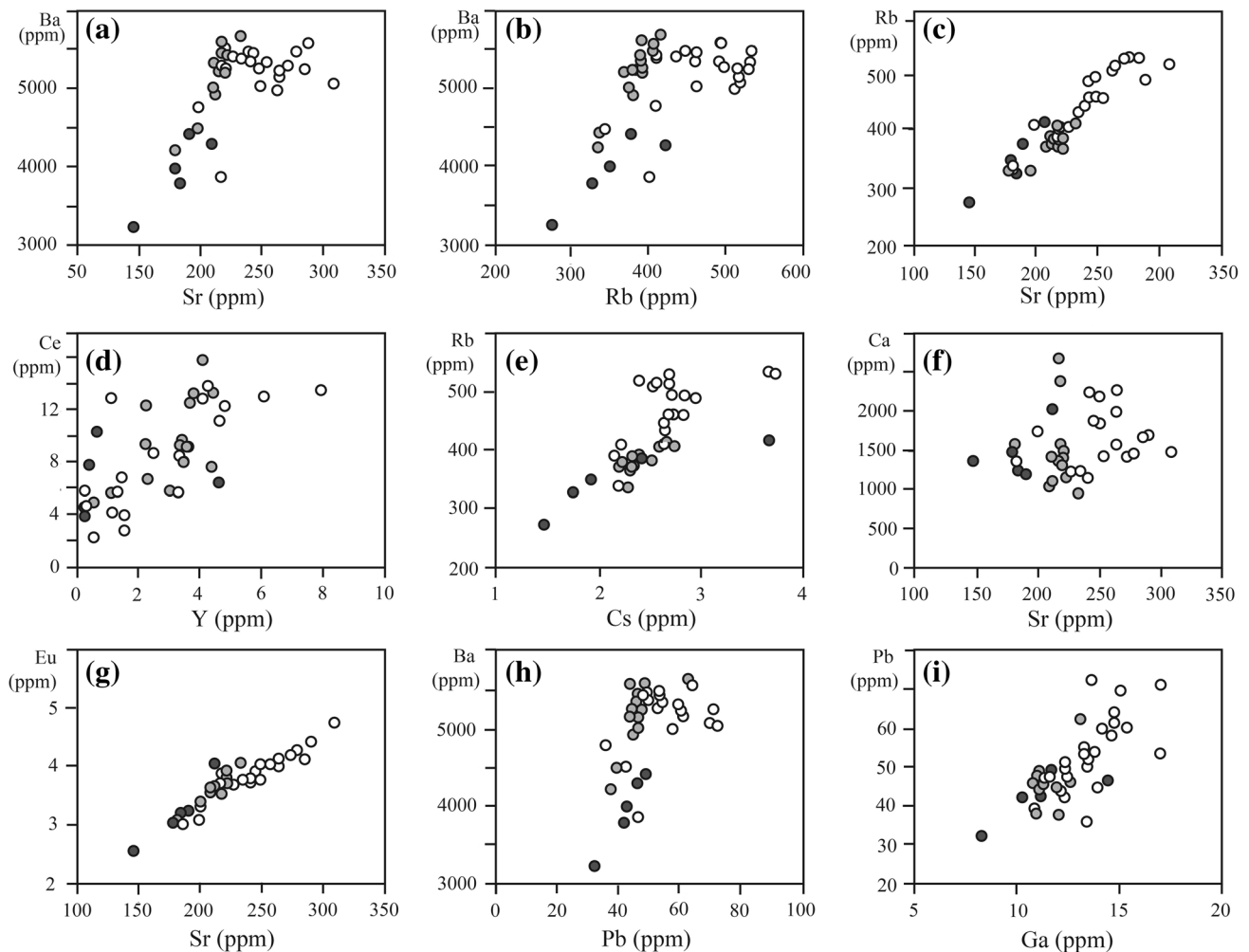


**Fig. 5** Relationship between compatible- and incompatible elements (concentration values taken from Table 1). *white circles* core, *light gray* middle zone, *dark gray* marginal zone

persistent elemental behavior during the entire crystal formation/transformation process is indicated. However, the plots (Fig. 6) display a saw-tooth pattern reflecting considerable scatter in H for which inclusions are only partly, and only in some spots, responsible. Information derived from 3D- and binary plots (Figs. 3, 5) does not entirely fit with some derived from the Hurst-exponent calculations.

Strontium and Ba plots are concordant along the traverse (Fig. 6). Rb behaves differently. A plot of H shows that in the core and in the adjacent inner middle zone (Fig. 6), Rb behaves inversely to Ba and Sr (spots 22–45), whereas in the outer middle- and marginal parts, the plots of all three elements are concordant. At the join of the middle- and marginal parts of the crystal (spot 8 adjacent to inclusion-filled spot 9), all three elements behave very chaotically (antipersistently); the H value attains a minimum.

To reveal the dynamics of element behavior in a more precise way, maps of maximum gradient values (Fig. 7a–c) and maps of direction of maximum gradient (Fig. 7d, e) were used. The maps of gradient value permit recognition of the areas where the changes in element concentration appear to have been most intensive. The maps of maximum gradient direction show in which direction the observed change is the greatest.

The maps of maximum gradient value (Fig. 7a–c) are dominated by the white stripes (high gradient) associated with major inclusions at spots 1–2, 6, 9, and 37–38–39. At these parts of the crystal, Ba, Sr, and Rb contents are changing most rapidly. Much lesser impact, not characteristic of the entire analyzed depth, can be observed for inclusions at spots 21, 26, and 30. Otherwise, all maps show a pattern of chaotically distributed microdomains for parts of the feldspar not perturbed by inclusions. The maps

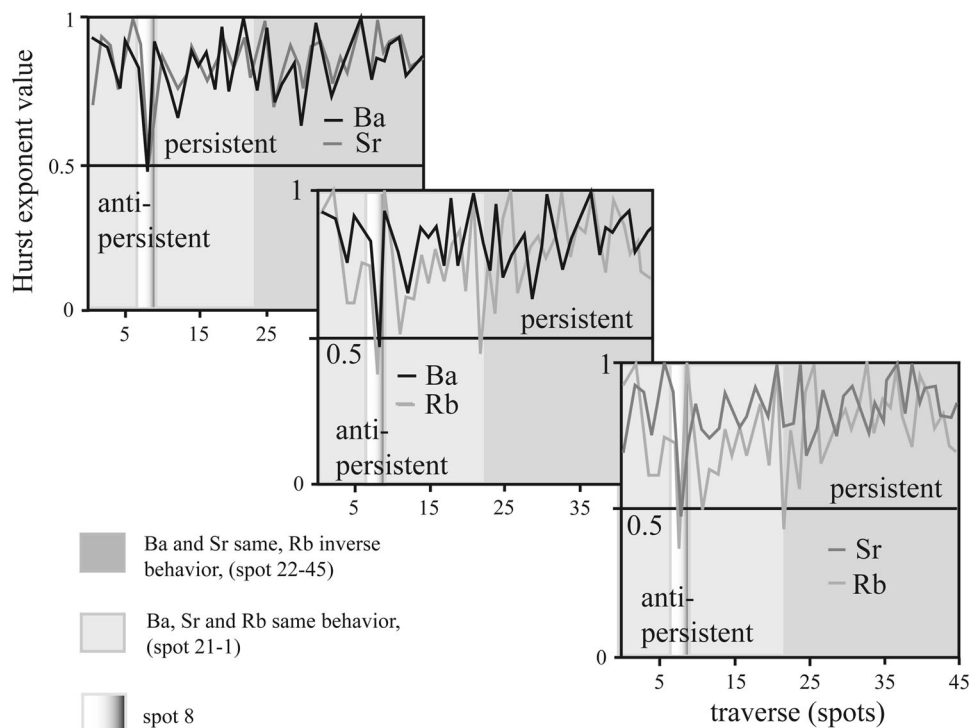


**Fig. 6** Behavior of elements during crystal growth. The Hurst-exponent diagrams show three phases of crystal growth. During crystallization of the core and of adjacent areas, all elements behave persistently with Rb behaving in an opposite manner to Sr and Ba.

of maximum gradient value comprise small, local, domains with higher gradient values each of which is surrounded by microdomains of reduced gradient value. Ba shows a chaotic pattern similar to that of Sr. Some areas in the middle part of the crystal are characterized by high degrees of gradient change. The least change is seen in the core between spots 45 and 38. A statistical comparison between gradient values of different elements normalized to the Ba dynamics reveals differences in their behavior (Table 2). The greatest gradient is shown by Rb; it reaches 111–120 % of the Ba dynamics for the interval without major inclusions (Table 2). Strontium shows the least degree of change at ~95 % that of Ba. This is consistent with the information derived from Hurst values.

Models of the direction of maximum gradient (Fig. 7d–i) show the direction of the greatest local decrease in concentration of an element. To simplify, the directions are grouped into four sectors with different colors. To reduce the possibility of bias, maps were doubled. Maps of the first set (Fig. 7d–f) have light and dark colors aligned along the Y axis of the models to highlight any pattern elements parallel to Y. The second set is of the same maps, but with an opposite alignment of the colors to highlight any potential pattern parallel to X (Fig. 7g–i). Again, clear order in the pattern is associated with inclusions only and

Further, growth involved persistent- and concordant Rb, Ba, Sr behavior. This regular pattern is broken by a sudden short change where all elements show antipersistent behavior

much more easily recognized on Fig. 7d–f. The direction of gradient change is precisely defined for inclusion-hosting spots, and for all spots immediately before and after. A similar effect is seen within the marginal zone of the crystal where the declining element content is well defined by a strong gradient orientation (Fig. 7d–f). For the spots that represent “pure” feldspar (spots 11–20), a lack of zoning is clearly visible with the most chaotic pattern characterizing the middle zone. The partly ordered pattern caused by inclusions seen on the maps of Fig. 7d–f is not visible on the maps of Fig. 7g–i which show randomly distributed microdomains. This difference signals that care is needed in sector assignment in order to decipher the signature of the process when using this method of data treatment.

To obtain a better insight into the relation between the Ba, Sr, and Rb distributions, correlations using cut-off level models and gradient models were used (Słaby et al. 2011; Śmigielski et al. 2012). These give a qualitative insight into the accordance of the behavior of the two elements being compared. The cut-off model comparison between two elements is based on simplifying the concentration distribution into only two areas: below- and above-average content. The degree of correlation is calculated as the percent of the areas of the two models that are accordant to

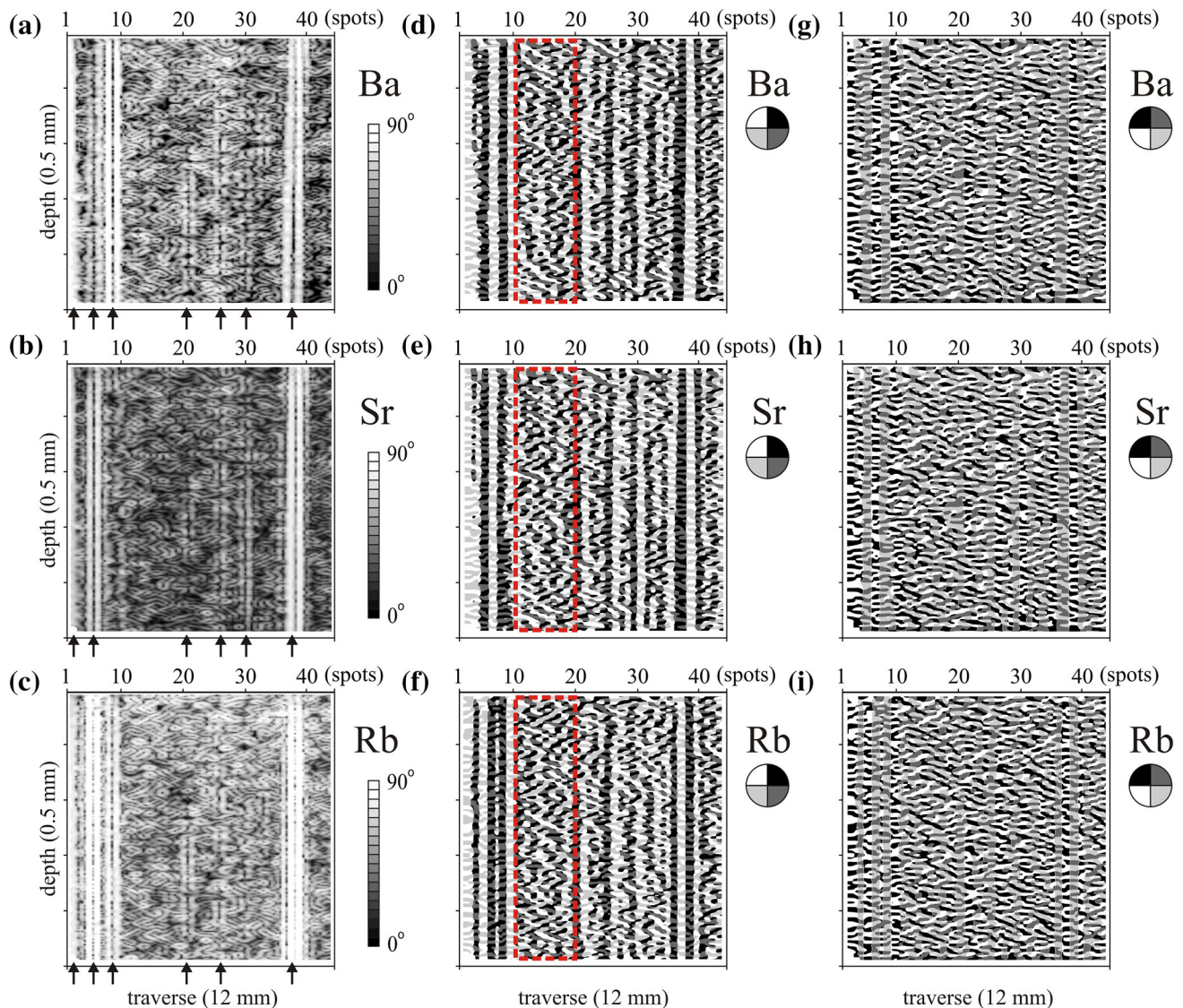


**Fig. 7** Spatial depiction of maximum gradient value (expressed as an angular value of the greatest rate of the concentration change of an element) (maps **a–c**) and of the direction of maximum gradient (expressed as the azimuth of the line of the greatest rate of change in the concentration of an element simplified to 4 sectors) (maps **d–f** and **g–i**). Please note that maps **a–c** Sr (**b**) and Rb (**c**) are in the same

vertical scale and thus their dynamics can be directly compared. The pattern is disturbed by inclusions within spots 1–2, 6–7, 9–10, 26, and 37–38–39 (marked with *arrows*). Undisturbed pattern of distribution in feldspar does not show any oscillatory zoning (marked with *rectangle*). See text for further explanation

each other. As the average level of Sr and Rb content varies across the analyzed portion of the crystal (Figure 1 electronic supplement), it is not possible to set a single value for the whole model. Thus, the results of the correlation for the 1–45 section are slightly biased and overestimated. For the whole model (spots 1–45), Ba, Sr and Rb contents of 5,100, 215, and 400 ppm, respectively, were used as averages. For selected portions representing less disturbed (11–36) or pure feldspar (11–20), the corresponding values used were 5,250, 218, and 385 ppm. The latter averages are fully representative of the analyzed portions of the crystal. The results are shown in Table 2 (electronic supplement).

In calculation, different 1 sigma error estimations were used. Only pairs of measurements where estimation of the correlation could be made with >85 % probability were taken into account. Thus, when the modeled error increases, the area of uncertainty also increases.

There is a clear accordance between contents of all three elements. If the content of one element is locally below average or above average, the probability of the other two behaving in a similar manner is very high. The highest accordance is between Ba and Sr. For feldspar free of inclusions, and after eliminating noise related to measurement uncertainty, accordance is between 90 and 99 %



**Table 2** Averaged dynamics of element concentration change calculated vertically and horizontally for spots from three parts of the analyzed crystal transect

Section	In-depth profile of spots			Along traverse		
	Ba	Sr	Rb	Ba	Sr	Rb
1–45	1.00	1.17	1.64	1.00	1.01	1.39
11–36	1.00	1.02	1.15	1.00	0.96	1.20
11–20	1.00	0.94	1.11	1.00	0.94	1.13

Values are presented in relation to barium dynamics for better comparison

(Table 2, electronic supplement). Although Rb is slightly less well correlated with these two elements, accordance is still high, between 72 and 86 %. Differences between Sr-Rb and Ba-Rb pairs are very small. The uncertainty level is smallest for Ba. This is because Sr- and Rb levels are typically very close to the average values, especially for the pure feldspar sections. In such cases, accurate estimation of the relation is not always possible because of measurement error.

The gradient model is based on the comparison of the relative change of the concentration of two elements measured in the direction of the general crystal growth—the X axis of the models. As in the case of the cut-off method, the concentration distribution is simplified into two groups, namely, increasing concentration and decreasing concentration and then compared. Such a model is free of potential bias linked to average-content estimation. However, this second approach does not have the same potential to average correlation over larger crystal areas as did the previous approach. It is also more sensitive to local gradients and local changes in element abundance. Thus, it is better at estimating local correlation, but more prone to analytical error.

As for the cut-off models, gradient changes of the all three elements are positively correlated. Where the content of one element is increasing, it is highly probable that the other two will do so also. Again, the Ba–Sr pair shows the highest estimated accordance of ~90 %. Accordance of the other two pairs is estimated at 70–90 % and is higher for inclusion-free parts of the crystal (Table 2, electronic supplement).

#### Crystal growth/re-growth morphology: CL data

A cathodoluminescence examination of the megacryst, of plagioclase inclusions within it, and of plagioclases surrounding it was performed. The megacryst shows a bluish, slightly patchy luminescence due to variable densities of Al–O<sup>−</sup>–Al structural defects (~450 nm CL emission; Finch and Klein 1999; Marfunin and Bershov 1970) and by differing contents of Fe<sup>3+</sup> activators (~700 nm CL emission; Götze et al. 2000; Figure 2c electronic supplement).

Areas close to dark-blue cracks are paler in color, pointing to a more defect-rich structure. The marginal part of the megacryst (spots 1–9) reveals the recrystallization process (Fig. 8a–c, e, f) that is imperceptible under the polarizing microscope. A mosaic of small alkali feldspar crystals shows a patchy luminescence pattern with a dark-blue color indicating relatively few defects (Fig. 8f). Nonrecrystallized parts of the megacryst (relics) close to the mosaic display a patchy pattern caused by irregular distributions, but increasing amounts of Al–O<sup>−</sup>–Al structural defects (Fig. 8e). Consequently, they are pale blue. Numerous inclusions of mica, plagioclase, and accessory minerals occur in the recrystallized areas (Fig. 8c, e, f).

The megacryst is surrounded by plagioclase of two generations that can be discriminated under CL by their differing intensity of green luminescence (Figure 2f, electronic supplement). Large, dark-green plagioclase is surrounded by smaller pale-green plagioclase crystals. The spectrum of the dark-green plagioclase matches that of the plagioclase inclusions hosted by the K-feldspar megacryst (Figure 2c, d, electronic supplement). Both have the same composition—An<sub>45</sub>Ab<sub>54</sub>Or<sub>1</sub>. The large dark-green plagioclase hosts numerous alkali feldspar inclusions with a common orientation—as with the alkali feldspar inclusions in plagioclase hosted by the megacryst. Smaller pale-green plagioclase crystals are more sodium-rich than the dark-green crystals and some show evidence of having grown into the darker plagioclase. Generally the pale-green generation is inclusion free though some long, blue, alkali feldspar needles or patches are spread across them (Figs. 8a, d; Figure 2b, electronic supplement). As alkali feldspar inclusions (Or<sub>0.5</sub>Ab<sub>5</sub>) are hosted by both the later-crystallized pale-green plagioclase and in the earlier dark-green plagioclase, the crystallization of the alkali feldspar inclusions seems to reflect a lack of equilibrium between the environment and the dark-green plagioclase, causing its partial dissolution. After re-equilibration, voids were healed by alkali feldspar. Dissolution and re-precipitation were probably contemporaneous with the growth of the second-generation, pale-green plagioclase.

Small plagioclase inclusions in the megacryst are homogeneous and show dark-green luminescence. They

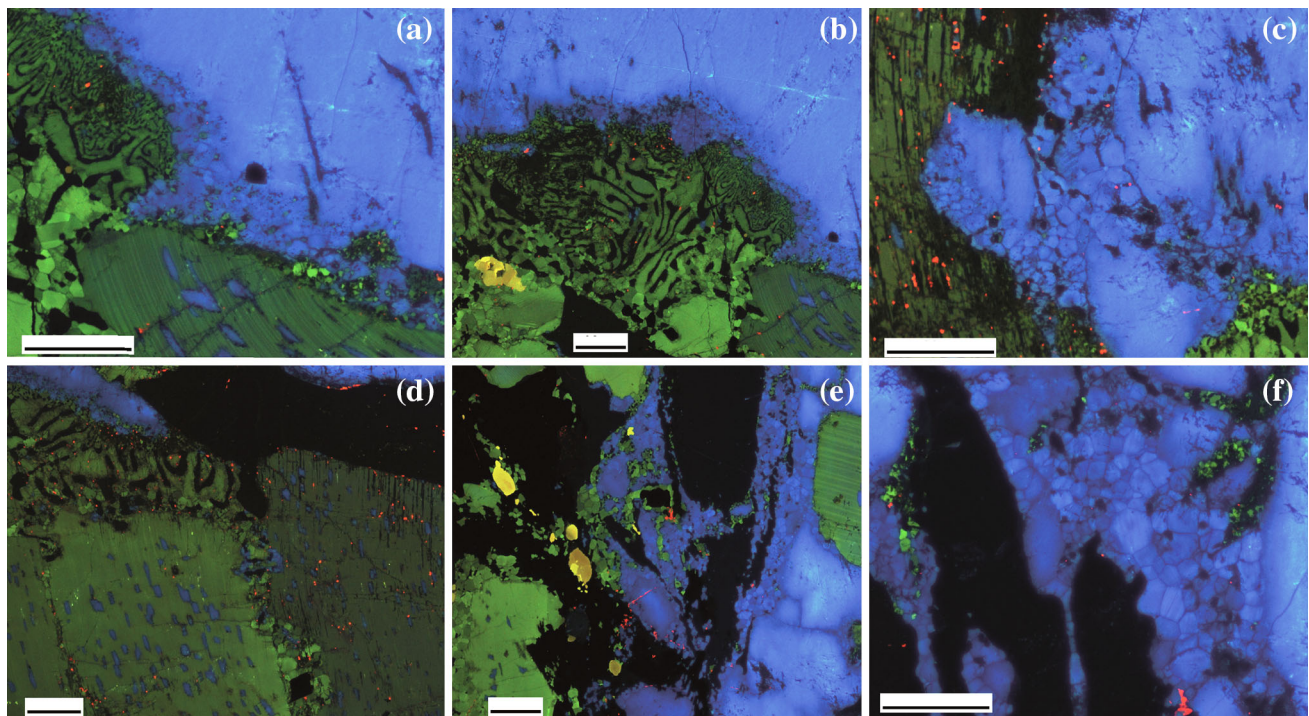


**Fig. 8** Dissolution–precipitation creep on the marginal part of the alkali feldspar megacryst. **a, b** Myrmekite bordered by narrow zones of newly formed alkali feldspars. Note the two generations of plagioclases, with dark- and pale-green luminescence, the latter showing mosaic development; **d** contact between dark-green and

pale-green plagioclase with evidence of dissolution–precipitation creep—mosaic of newly formed plagioclases and some alkali feldspars crystallizing in the dissolved plagioclase parts; **c, e, f** recrystallized zones of alkali feldspar megacryst

are full of irregular, small spots of alkali feldspar (Fig. 8a; Figure 2a, e electronic supplement) displaying a common orientation and having potassium-rich composition ( $Or_{95}Ab_5$ ). The plagioclase inclusions have reaction rims with myrmekitic intergrowths. Small carbonate crystals occur sporadically.

Myrmekite is intensively developed in the margins of the megacryst (Fig. 8a, b). Plagioclase in the myrmekite intergrowths shows pale-green luminescence. Commonly, myrmekites are surrounded by mosaics of pale-green plagioclase. Similar small crystals also occur at contacts between larger plagioclase crystals or at the borders of dark-green plagioclase. A formation by dissolution–precipitation creep is indicated (Fig. 8d).

#### Structural changes: Raman spectroscopic maps

To track structural changes, a total of twenty-six Raman spectroscopic analyses were performed on the recrystallized margin of the crystal and on areas close to cracks and within relatively homogeneous areas weakly affected by strain. Selected Raman spectra and maps resulting from k-means cluster analysis are shown on figures 9 and 3 (electronic supplement).

The measured band positions and relative intensities are consistent with the chemical composition of alkali feldspar. Changes are clearly reflected in slight shifts of band positions and in the widths and intensities of bands. Based on the data of Stengel (1977), special attention was paid to triplet bands at about  $514$ ,  $480$ , and  $455\text{ cm}^{-1}$  (symmetric T–O stretch and O–T–O deformation modes in  $TO_4$  groups),  $290\text{ cm}^{-1}$  (O–T–O deformation and T–O–T lattice modes) and below  $290\text{ cm}^{-1}$  (T–O–T and M–O modes). Features in all these regions in the spectra differ for slightly strained-, cracked- and recrystallized-megacryst domains.

A k-means cluster analysis of the relatively unchanged domains shows that the relationship between  $480$  and  $455\text{ cm}^{-1}$  in the triplet is similar in all classes (Fig. 9a). The intensity of the bands varies to a small extent. In cracked areas, the same relationship is very variable (Fig. 9b). The changes were quantified using ratios of the intensities of the triplet bands. For the orthoclase standard (Fabel et al. 1972), the calculated ratios are  $I_{480}/I_{455} = 1.39$ ,  $I_{515}/I_{455} = 5.01$ , and  $I_{515}/I_{480} = 3.61$ . Calculation details are given in Table 3–5 (electronic supplement). Deviation from the standard values is taken as an indicator of deformation modes in  $TO_4$  groups in individual

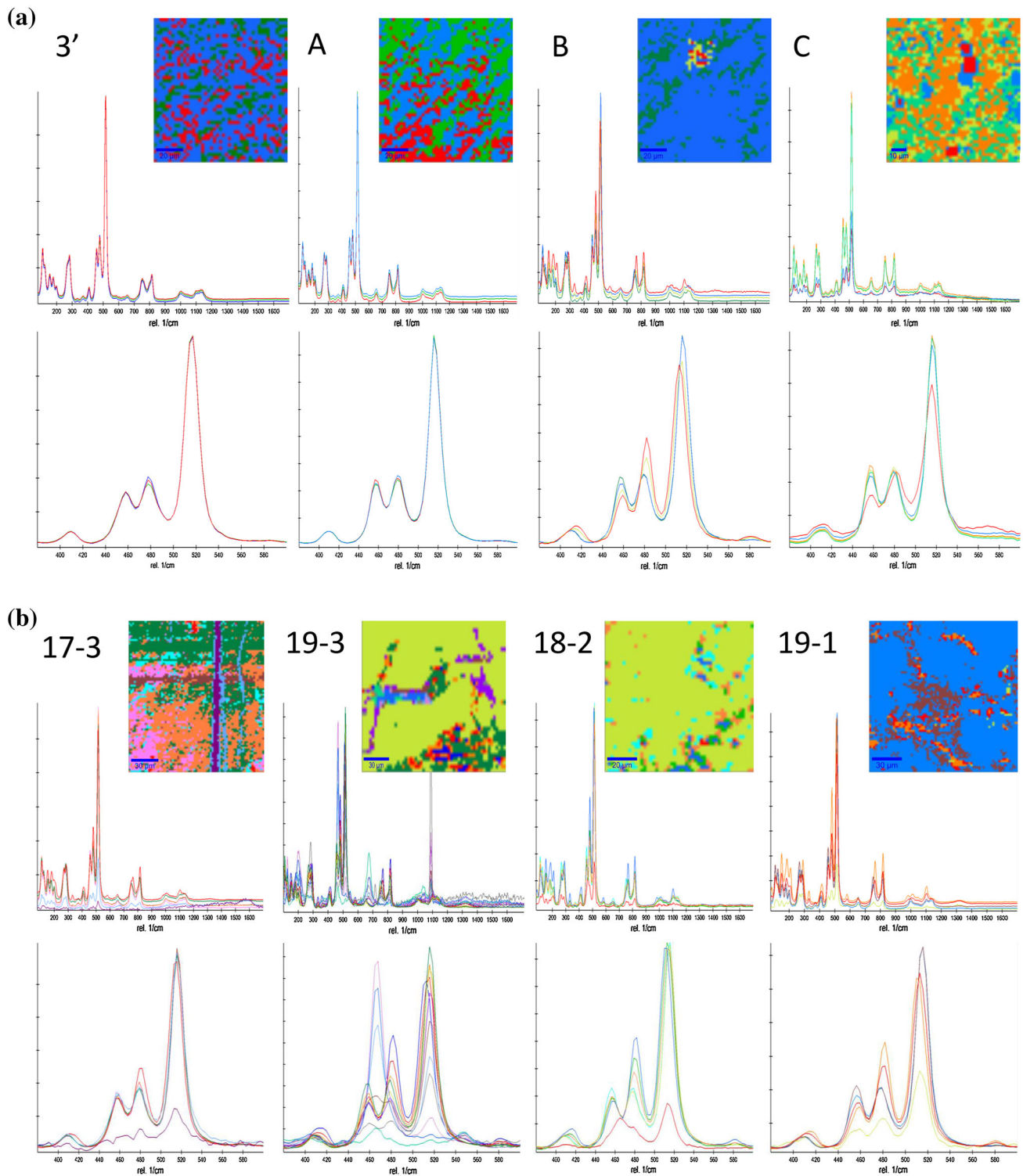


**Fig. 9** Raman spectra and maps of K-means cluster analysis. **a** Relatively undeformed regions, **b** cracked regions, and **c** recrystallized marginal part of alkali feldspar. Numbers and letters next to maps are feldspar areas abbreviation (see also Table 6, electronic supplement)

domains (Table 6, electronic supplement). This table also shows the ranges of integration areas for selected Raman bands. The more a domain is affected by strain, the more

patchy is the k-means cluster map and the greater the number of classes (compare Table 6, electronic supplement and Fig. 9b). Almost all calculated ratios (Table 6,



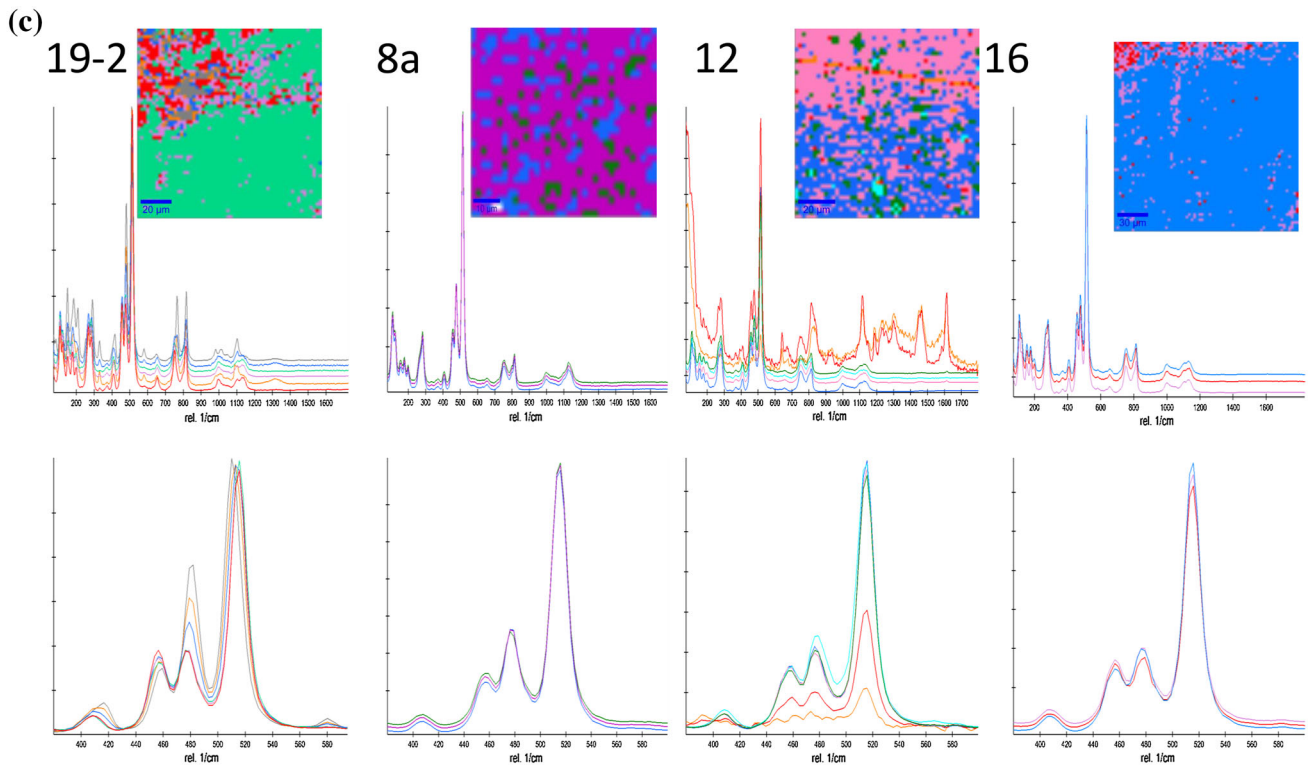


Fig. 9 continued

electronic supplement) deviate from the standard, indicating that the structure of almost all domains is distorted. The value of  $I_{515}/I_{480}$  is always below the standard, pointing to a constant growth of the  $480\text{ cm}^{-1}$  peak during the transformation process. In contrast, the intensity of the  $455\text{ cm}^{-1}$  peak decreases within the strained domains. This peak is indicative of order–disorder in feldspar. Its decrease in relation to the  $480$  and  $515\text{ cm}^{-1}$  bands suggests increasing disorder in the structure of these areas. Order–disorder in the feldspar structure is associated with Al–Si distribution in the tetrahedra. Changes in Al–Si order were investigated based on intensities of examined bands. The intensity of the bands is proportional to the polarizability tensor of the corresponding vibration. Bond Si–O–Al is slightly polarized, resulting in a relatively large change in the polarizability of the stretching and bending oscillations of the bond and in the higher intensity of the corresponding band in the Raman spectrum. The presence of T–O stretch- and O–T–O deformation modes in the  $\text{TO}_4$  group does not indicate that the mineral itself is deformed. The declining  $455\text{ cm}^{-1}$  band suggests that the Al and all three Si are disordered.

Additionally, some structural changes are observed based on the bands grouped around  $290\text{ cm}^{-1}$  (O–T–O and T–O–T deformations). Quantification of the changes within this area was carried out using  $I_{266}/I_{288}$  (0.69 for standard

orthoclase;  $266\text{ cm}^{-1}$  due to O–T–O deformations and T–O–T lattice modes). In strained domains, the value of this ratio grows. Analysis of band areas indicates a decrease of the value of  $I_{266}/I_{288}$  which correlates perfectly with increasing  $I_{515}/I_{455}$ . The decrease in  $I_{266}/I_{290}$  is the result of an increase of the  $290\text{ cm}^{-1}$  band and a subtle decrease of the  $266\text{ cm}^{-1}$  band. The correlation is linear. Increasing  $\sim 290\text{ cm}^{-1}$  band intensity correlates with the appearance of the  $\sim 331\text{ cm}^{-1}$  band, the declining  $110\text{ cm}^{-1}$  band, and the disappearance of  $124\text{ cm}^{-1}$  band—in the case of the latter two, the result of T–O–T & M–O lattice vibration, where  $M = \text{K, Na, Ca}$ . The bands at  $176$ ,  $200$  and  $285\text{ cm}^{-1}$  are slightly shifted to  $184$ ,  $209$  and  $290\text{ cm}^{-1}$ , respectively. A very weak (but with good S/N)  $85\text{ cm}^{-1}$  band appears. The recrystallized areas show some mixed characteristics, some with an affinity to the cracked areas, some to less-strained, more homogeneous areas (Fig. 9c). The reason lies in the diverse sizes and mutual orientations of small recrystallized areas.

## Discussion

The growth/re-growth of the megacryst does not encompass the span of time during which its growth host rock formed nor can it definitively aid in the recognition of the

current host rock. Nevertheless, the chemical composition and the growth and re-growth textures of the megacryst register many important events in the evolution and deformation of the rock. The present study does not contradict the commonly held view that alkali feldspar does not effectively trace deformation events during protomylonite development (Vernon et al. 1983; Vernon and Flood 1988; Vernon 2004), but draws attention to the fact that subtle changes are open to recognition with the help of multimethod approach.

The history of the megacryst records different stages in its formation that reflect changes in the composition of its crystallization environment and the dynamics of element incorporation. The stages can be defined on the basis of the relation between more homogeneous or heterogeneous element distribution (also gradient distribution), similar or different degrees of persistency in the manner of element incorporation and its later diffusion within the crystal lattice. The reconstruction of every single stage will be more effectively aided using a combination of data-processing tools rather than any single one. This becomes evident if the data from element distribution maps and derivative maps are compared with Hurst-exponent values. Even where change in the dynamics of crystallization did not obviously affect the pattern of elemental distribution, it is reflected in Hurst values. Hurst values reveal hidden features of the overlapping processes. In the present study, relationships between a number of data sets enabled at least three different stages of crystal formation/transformation to be distinguished, namely, core, middle zone, and marginal zone (mosaic of crystals). In addition, small changes enabled the recognition of some subzones within the core and the middle zone. Inclusions that attached to or nucleated on, the growing feldspar surface delimit the range of the subzones.

The core area of the megacryst shows the most homogeneous distribution of elements. The dynamics of element behavior was, however, different for different elements. Persistency is the same for Ba and Sr, the inverse for Rb. The changeable Rb dynamics may reflect its greater mobility in the melt compared with that of Ba and Sr (Perugini et al. 2006, 2008) and the influence of the contemporaneous crystallization of other phases on Rb incorporation. At the same time, Rb and Sr incorporation into the megacryst are fully coupled. Inclusions of plagioclase in the megacryst may indicate the simultaneous growth of both phases with the preferred introduction of Sr into the plagioclase as the partition coefficient for Sr is higher for plagioclase than for alkali feldspar. Simultaneous crystallization of some phases requires an appropriate distribution of trace elements between all of them. In the megacryst, decoupling of Ba from Sr between the core and middle zone is evident. Values of the Hurst exponent calculated

for the Ba and Sr data series point to similar, though noisy, degrees of persistency during the crystallization process.

The relationships between Sr, Rb, and Ba show that Ba is incorporated in excess of the other elements. In the crystal core, the Ba content does not change during fractionation, whereas those of the other elements do. The remaining elements, especially incompatible elements, obey Henry's rule during differentiation (Fig. 5). Barium behavior in the crystal core cannot be explained by a substitution scheme and its relation to Al–O<sup>−</sup>–Al defects (Słaby et al. 2008). Generally, Ba incorporation follows the KSi–BaAl vector. Barium may also substitute for Ca (Mahood and Stimac 1990; Blundy and Wood 1991) as may LREE (Ren 2004). Ba (Sr, LREE)–Ca substitution is charge balanced by Al. Increasing Al–O<sup>−</sup>–Al defect density may influence Ba reorganization within the middle part of the crystal, although not in the crystal core where the defect density is very low. As Sr is associated with Ba in the feldspar structure, Ba reorganization will entail Sr reorganization.

Generally, the megacryst core preserves features of the magmatic environment. The crystal structure of the core area is almost unchanged (Fig. 9). The heterogeneous, patchy element distribution pattern of the middle zone is difficult to explain by magmatic differentiation. If the melt was viscous and diffusion not efficient enough to provide equilibration conditions close to the crystal surface, the expected pattern would be similar to that formed by self-organization of the melt. This is not the case here; no subtle oscillation in the crystal growth morphology is seen. At the same time, the patchy pattern is supported by gradient maps. Gradient change within small domains can reflect reorganization of the element distribution in the crystal lattice, which also influences Hurst values. The diagram of the exponent should be smoother if the data series are the result of magmatic crystallization alone.

The conditions of mylonitization in the Kuršiai pluton were ~700 °C and ~7 kbars (Skridlaitė and Smilgienė 2004). It is questionable whether, under such circumstances, the crystal perfectly preserves its original magmatic trace-element distribution. Digital concentration-distribution models (DC-DM) and derivative gradient models show arrays that crystallization from a melt can only partly explain. Fractal statistics, e.g., Hurst-exponent values demonstrate changing dynamics that are difficult to explain in the light of the almost constant level of element concentration during magmatic crystallization. Thus, the Raman and CL data may prove helpful.

As do the trace-element distribution pattern and gradient maps, the Raman study reveals an arrangement of microdomains in the feldspar showing different degrees of order-disorder. The estimated temperature of the mylonitization was high and prevented increased structural ordering. In

fact, the Raman spectra collected within cracked/strained areas suggest increasing disorder. The intensity of the band at  $455\text{ cm}^{-1}$ , indicative of order–disorder in feldspar, decreases within these domains. The three structural types of potassium feldspar (microcline, orthoclase and sanidine) display increasing structural disorder in the distribution of the one Al and three Si cations within the rings of four-linked tetrahedra of the feldspar lattice. Maximum microcline has the highest degree of Si–Al ordering, with the Al cation occurring at a unique tetrahedral site and the Si cations in the remaining tetrahedral sites (Freeman et al. 2008). Raman bands are primarily sensitive to changes in polarizability of the bonds. The intensity of the bands is proportional to the polarizability tensor of the corresponding vibration. As Raman modes increase in intensity as the bonds become more asymmetric, a T–O–T mode become stronger for Si–O–Al than for Al–O–Al linkages. Therefore, the increasing intensity of the  $290\text{ cm}^{-1}$  band, indicating an increasing disorder, indicates a decreasing lattice symmetry because of changes in T–O–T linkages (Si–O–Al predominate over Al–O–Al linkages). Observed disorders and changes in T–O–T linkages may reflect diffusion (Svahnberg and Piazzolo 2013). As a consequence of exchange of Al for Si in the T–O–T linkages, change in the lattice symmetry (further electronegativity of Al and Si) is observed that results in deformation arising from a change in the T–O–T bond polarizability. An increase of the polarizability tensor (selection rule in Raman spectroscopy) leads to a higher intensity of the selected Raman bands. Decreasing  $I_{266}/I_{282}$  and increasing  $I_{515}/I_{455}$  show increasing disorder that does not reflect a greater proportion of Al–O–Al linkages in the mineral structure but rather changes is the symmetry of the T–O–T due to the presence of the more electronegative atom in T–O–T linkages.

Cathodoluminescence also reveals increased numbers of Al–O<sup>−</sup>–Al defects within strained, cracked crystal regions—an effect that can reflect small amounts of water in the feldspar or extensive Ba incorporation into the structure (Słaby et al. 2008, 2009). Here the latter is not relevant except for small-scale Ba reorganization. Micas, water-bearing minerals, are abundant in the system. Traces of carbonates point to CO<sub>2</sub> presence in the fluid during the protomylonitization. Feldspars, nominally anhydrous, carry variable amounts of water. On the one hand, water heals and rearranges Al–O<sup>−</sup>–Al defects (Finch and Klein 1999; Graham and Elphick 1990, 1991; Słaby et al. 2009) and, on the other, commonly promotes hydroxyl defects (Kronenberg et al. 1996) that trigger significant redistributions among sites, thus increasing diffusion. Water also substitutes for K sites favored by Rb (Kronenberg et al. 1996). Rybacki and Dresen (2004) noted that the predominance of diffusion-controlled creep in mylonites occurs at grain sizes of about 0.1–1 mm, much smaller than the

investigated megacryst. The process is dependent on temperature, stress, and feldspar composition. Casini et al. (2009) indicated that diffusional creep during recrystallization in the presence of water-rich fluid can occur even at low temperatures.

In the megacryst, minor reorganization of element distributions, especially Rb, is evident. The distribution of Rb, the gradient map, and Hurst values all indicate the dynamic, chaotic behavior of this element. The gradient map also indicates considerable Ba reorganization. A geochemical pattern which could result from magmatic crystallization was changed into a pattern of chaotically distributed microdomains, probably reflecting the local mobilization of Ba, Sr, and Rb. Local depletion or increase of element concentration will blur an initial distribution, replacing it with local minima and maxima and causing both average contents and gradients for all elements to be of high accordance (Table 2 electronic supplement). However, the obvious weaker accordance for Rb than for the Ba/Sr pair could easily result from high Rb mobility.

Imperfections in the crystal lattice can promote elemental redistribution. Minor changes in the original elemental distribution pattern may also reflect structural changes by a process similar to a small-scale diffusion creep, i.e., diffusion through vacancies and defects in the crystal lattice.

During the formation of the protomylonite, some changes related to dissolution–precipitation creep occurred. A mosaic of crystals, possibly growing in continuity with the parent megacryst, changed the pattern of the trace-element distribution in the marginal part of the megacryst. A minor amount of biotite and carbonate accompanied the process and point to the presence of fluid which can promote dissolution–precipitation creep. Differences in the mode and dynamics of element incorporation into the mosaic crystals are recognized by the distribution models, gradient maps, and Hurst-exponent values. Dissolution–precipitation creep introduces abrupt change as indicated by the partly anti-persistent element behavior in the more dynamic environment of inclusion-rich domains beyond spot 9. In the inclusion-rich spot 9, all elements behave persistently. The inclusions were apparently attached to the alkali feldspar surface during dissolution–precipitation. In the subsequent megacryst domain, all of the chosen elements show extreme chaotic behavior (spot 8) and, outwards, the concentrations of all decrease markedly toward the recrystallized margin. The dissolution–precipitation creep probably followed myrmekite formation and had wider range significance than creating a mosaic of the crystals. Cathodoluminescence reveals two generations of plagioclase. Plagioclase with a pale-green luminescence correlates with the products of myrmekite reaction. Both pale- and dark-green plagioclases contain alkali feldspar inclusions with a



composition similar to that of crystals formed due to dissolution–precipitation creep on the megacryst margin. Their formation should be contemporaneous with the crystal mosaic.

## Conclusions

A K-feldspar megacryst reveals a part of the formation/deformation history of its host rock. The rock mineral and chemical composition reflects overlapping magmatic- and metamorphic processes. The latter relate to the initial stage of mylonitization—protomylonitization. The recognition of subtle changes to the geochemical pattern of the alkali feldspar due to the protomylonitization is not easy. Alkali feldspar from the protomylonite does not show much outward sign of change. The only visible changes are cracks. In contrast, the use of multiple methods and the many different data sets acquired shows that almost no part of the crystal retains the original distribution of elements in the crystal structure. Even the very beginning of the mylonitization process can lead to subtle reorganization on the trace-element distribution and to the recrystallization of some parts of the crystal. Thus, feldspars are shown to be extremely sensitive indicators of both magmatic- and metamorphic processes. Because the changes are subtle, verifications provided by the different data sets give confidence that the results are not spurious. In this, correct data processing plays a major role.

New methods of data processing combining digital models of element distribution, derivative gradient models, fractal statistics, and Raman- and CL studies that give a precise insight into the protomylonite history are presented. In a system involving multiple interactions and in which any resulting geochemical imprint fails to define a credible evolutionary path, a multimethod approach may be the key to any robust petrogenetic interpretation. A reliable understanding of the rock's origin may derive from the precise and thorough analysis of a single phase. Here, such an approach helped to identify structural changes and changes in primary magmatic element distribution patterns caused by deformation. The identification of new methods of data retrieval and processing is of special importance in this context.

**Acknowledgments** We are grateful to two anonymous reviewers for their critical reviews, as well as to Jochen Hoefs for editorial handling. Our thanks go to Svetlana Bogdanova and Gražina Skridlaite and Tomasz Śmigielski for inspired discussion. The work was funded by NCN 2011/01/B/ST10/04541. Pádhraig Kennan (University College Dublin) and Raymond Macdonald (IGMP University of Warsaw) helped with English language. One of the Authors (KM) acknowledges the following institutions for supporting her PhD position: the European Regional Development Fund under the Innovative Economy Programme (grant coordinated by JCET-UJ, No

POIG.01.01.02-00-069/09), “Molecular sciences for medicine” (co-financed by the European Social Fund within the Human Capital Operational Programme) and the Marian Smoluchowski Kraków Research Consortium: “Matter-Energy-Future” (Granted KNOW status for 2012–2017 by the Ministry of Science and Higher Education).

**Open Access** This article is distributed under the terms of the Creative Commons Attribution License which permits any use, distribution, and reproduction in any medium, provided the original author(s) and the source are credited.

## References

- Blundy J, Wood B (1991) Crystal–chemical control on the partitioning of Sr and Ba between plagioclase feldspar, silicate melts, and hydrothermal solutions. *Geochim Cosmochim Acta* 55:193–209
- Bogdanova S, Gorbatshev, Grad M, Janik T, Guterch A, Kozlovskaya E, Motuza G, Skridlaite, Starostenko V, Taran L, EUROBRIDGE and Polonaise Working Groups (2006) EUROBRIDGE: new insight into the geodynamic evolution of the East European Craton. In: Gee DG, Stephenson RA (eds) *European lithosphere dynamics*, vol 32. Geological Society, London, pp. 599–625
- Bucher K, Grapes R (2011) *Petrogenesis of metamorphic rocks*. Springer, Berlin, p 440
- Carroll SA, Knauss KG (2005) Dependence of labradorite dissolution kinetics on CO<sub>2</sub>(aq), Al(aq) and temperature. *Chemica Geol* 105:137–162
- Casini DJ, Senserini P, Oggiano G (2009) Evidence for water-assisted diffusion creep in the mylonitic gneisses of Giuncana, northern Sardinia, Italy. *Trabajos de Geología, Universidad de Oviedo* 29:157–163
- Cherniak DJ (1996) Strontium diffusion in sanidine and albite, and general comments on Sr diffusion in alkali feldspars. *Geochim Cosmochim Acta* 60:503–543
- Cherniak DJ (2002) Ba diffusion in feldspar. *Geochim Cosmochim Acta* 66:1641–1650
- Claesson S, Bogdanova S, Bibikova EV, Gorbatshev R (2001) Isotopic evidence for Paleoproterozoic accretion in the basement of the East European Craton. *Tectonophysics* 339:1–18
- Cooper GRJ (2003) Feature detection using sun shading. *Comput Geosci* 29:941–948
- Domonik A, Słaby E, Śmigielski M (2010) The Hurst exponent as a tool for the description of magma field heterogeneity reflected in the geochemistry of growing crystals. *Acta Geol Pol* 60:437–443
- Ewart A, Griffin WL (1994) Application of proton-microprobe data to trace-element partitioning in volcanic-rocks. *Chem Geol* 117:251–284
- Fabel GW, White WB, White EW, Roy R (1972) Structure of lunar glasses by Raman and soft X-ray spectroscopy. In: *Proceedings of the third lunar science conference*. Supplement 3, *Geochimica et Cosmochimica Acta* 1, pp 939–951
- Finch AA, Klein J (1999) The causes and petrological significance of cathodoluminescence emissions from alkali feldspar. *Contrib Miner Petrol* 135:234–243
- Freeman JJ, Wang A, Kuebler KE, Jollif BL, Haskin LA (2008) Characterization of natural feldspars by Raman spectroscopy for future planetary exploration. *Can Mineral* 46:1477–1500
- Giletti BJ (1991) Rb and Sr diffusion in alkali feldspars, with implications for cooling histories of rocks. *Geochim Cosmochim Acta* 55:1331–1343
- Ginibre C, Wörner G, Kronz A (2004) Structure and dynamics of the Laacher See magma chamber (Eifel, Germany) from major and

- trace element zoning in sanidine: a cathodoluminescence and electron microprobe study. *J Petrol* 45:2197–2223
- Ginibre C, Wörner G, Kronz A (2007) Crystal zoning as an archive for magma evolution. *Elements* 3:261–266
- Götze J, Krbetschek MR, Habermann D, Wolf D (2000) High-resolution cathodoluminescence of feldspar minerals. In: Pagel M, Barbin V, Blanc P, Ohnenstetter D (eds) *Cathodoluminescence in geosciences*. Springer, Berlin, pp 245–270
- Graham CM, Elphick SC (1990) A re-examination of the role of hydrogen in Al-Si interdiffusion in feldspars. *Contrib Mineral Petrol* 104:481–491
- Graham CM, Elphick SC (1991) Some experimental constraints on the role of hydrogen in oxygen and hydrogen diffusion and Al-Si interdiffusion in silicates. In: Ganguly J (ed) *Diffusion and flow in minerals and fluids, advances in physical chemistry*, vol 8. Springer, New York, pp 248–285
- Gringarten E, Deutsch CV (2001) Teacher's aide variogram interpretation and modeling. *Math Geol* 33:507–534
- Icenhower J, London D (1996) Experimental partitioning of Rb, Cs, Sr, and Ba between alkali feldspar and peraluminous melt. *Am Mineral* 81:719–734
- Ishii K, Kanagawa K, Shigematsu N, Okudaira T (2007) High ductility of K-feldspar and development of granitic banded ultramylonite in the Ryoke metamorphic belt, SW Japan. *J Struct Geol* 29:1083–1098
- Knesel KM, Davidson JP, Duffield WA (1999) Open-system evolution of silicic magma by assimilation followed by recharge: evidence from Sr isotopes in sanidine phenocrysts, Taylor Creek rhyolite, NM. *J Petrol* 40:773–786
- Kronenberg AK, Yund RA, Rossman GR (1996) Stationary and mobile hydrogen defects in potassium feldspar. *Geochim Cosmochim Acta* 60:4075–4094
- Lahtinen R, Garde AA, Melezhik V (2008) Palaeoproterozoic evolution of Fennoscandia and Greenland. *Episodes* 31:20–28
- Mahood GA, Stimac JA (1990) Trace-element partitioning in pantellerites and trachytes. *Geochim Cosmochim Acta* 54:2257–2276
- Mandelbrot BB, Van Ness JW (1968) Fractional Brownian motions, fractional noises and applications. *SIAM Rev* 10:442
- Marfunin AS, Bershov LV (1970) Electron-hole centers in feldspars and their possible crystallochemical and petrological significance (in Russian). *Dokl Akad Nauk SSSR* 193:412–414
- Matheron G (1963) Principles of geostatistics. *Econ Geol* 58:1246–1266
- Menegon L, Pennacchioni G, Spiess R (2008) Dissolution-precipitation creep of K-feldspar in mid-crustal granite mylonites. *J Struct Geol* 30:565–579
- Motuz G (2005) Structure and formation of the crystalline crust in Lithuania. *Mineral Soc Poland Spec Pap* 26:69–79
- Motuz G, Staškus V (2009) The oldest Lithuanian rocks. *Geologijos akiračiai* (Journal of the Geological Society of Lithuania) 3–4:41–47
- Motuz G, Motuz V, Salnikova E, Kotov A (2008) Extensive charnockitic-granitic magmatism in the crystalline crust of West Lithuania. *Geologija* 61:1–16
- Nash WP, Crecraft HR (1985) Partition coefficients for trace elements in silicic magmas. *Geochim Cosmochim Acta* 49:2309–2322
- Neuser RD, Bruhn F, Götze J, Habermann D, Richter DK (1995) Kathodolumineszenz: Methodik und Anwendung. *Zentralblatt für Geologie und Paläontologie Teil I, H. 1(2)*:287–306
- Nironen M (1997) The svekofennian orogen: a tectonic model. *Precamb Res* 86:21–44
- Perini G, Tepley FJ, Davidson JP, Conticelli S (2003) K-feldspar megacrysts hosted in alkaline potassic rocks from central Italy: a track for low-pressure processes in mafic magma. *Lithos* 66:223–240
- Perugini D, Petrelli M, Poli G (2006) Diffusive fractionation of trace elements by chaotic mixing of magmas. *Earth Planet Sci Lett* 243:669–680
- Perugini D, De Campos CP, Dingwell DB, Petrelli M, Poli D (2008) Trace element mobility during magma mixing: preliminary experimental results. *Chem Geol* 256:146–157
- Peters EE (1994) *Fractal market analysis: applying chaos theory to investment and economics*. Wiley, New York, p 315
- Ren M (2004) Partitioning of Sr, Ba, Rb, Y, and LREE between alkali feldspar and peraluminous silicic magma. *Am Mineral* 89:1290–1303
- Rybacki E, Dresen G (2004) Deformation mechanism maps for feldspar rocks. *Tectonophysics* 382:173–187
- Schulmann K, Melka R, Mlcoch B (1996) High-temperature microstructures and rheology of deformed granite, Erzgebirge, Bohemian Massif. *J Struct Geol* 18:719–733
- Simpson C, Wintsch RP (1989) Evidence for deformation-induced K-feldspar replacement by myrmekite. *J Metamorph Geol* 7:261–275
- Skridlaitė G, Smilgienė Z (2004) Evolution of metamorphism and tectonic conditions. In: Baltrūnas V (ed) *Evolution of earth crust and resources in Lithuania, Vilnius*, pp 40–46 (in Lithuanian)
- Skridlaitė G, Whitehouse M, Rimša A (2007) Evidence for a pulse of 1.45 Ga anorthosite–mangerite–charnockite–granite (AMCG) plutonism in Lithuania: implications for the Mesoproterozoic evolution of the East European Craton. *Terra Nova* 19:294–301
- Skridlaitė G, Bagiński B, Whitehouse M (2008) Significance of ~1.5 Ga zircon and monazite ages from charnockites in southern Lithuania and NE Poland. *Gondwana Res* 14:663–674
- Skridlaitė G, Bagiński B, Bogdanova S, Whitehouse M (2010) Metamorphism and magmatism in the western East European Craton: implications for 1.84 to 1.45 Ga evolution in Lithuania. *Geophysical Research Abstract* 12, EGU2010
- Słaby E, Galbarczyk-Gąsiorowska L, Seltmann R, Müller A (2007a) Alkali feldspar megacryst growth: geochemical modelling. *Mineral Petrol* 68:1–29
- Słaby E, Seltmann R, Kober B, Müller A, Galbarczyk-Gąsiorowska L, Jeffries T (2007b) LREE distribution patterns in zoned alkali feldspar megacrysts—implication for parental melt composition. *Mineral Mag* 71:193–217
- Słaby E, Götze J, Wörner G, Simon K, Wrzalik R, Śmigielski M (2008) K-feldspar phenocrysts in microgranular magmatic enclaves: a cathodoluminescence and geochemical study of crystal growth as a marker of magma mingling dynamics. *Lithos* 105:85–97
- Słaby E, Götze J, Wörner G, Simon K, Wrzalik R, Śmigielski M (2009) Order-disorder in K-feldspar grown from mixed magmas—CL and Raman study. *Conference on micro-Raman spectroscopy and luminescence studies of the earth and planetary sciences (Corals I)* April 2–4, 2009 Mainz, Germany, #3003
- Słaby E, Śmigielski M, Śmigielski T, Dmonik A, Simon K, Kronz A (2011) Chaotic three-dimensional distribution of Ba, Rb and Sr in feldspar megacrysts grown in an open magmatic system. *Contrib Mineral Petrol* 162:909–927
- Słaby E, Martin H, Hamada M, Śmigielski M, Dmonik A, Götze J, Hoefs J, Hałas S, Simon K, Devidal J-L, Moyen JF, Jayananda M (2012) Evidence in Archaean alkali-feldspar megacrysts for high temperature interaction with mantle fluids. *J Petrol* 53:909–927
- Śmigielski M, Słaby E, Dmonik A (2012) Digital concentration-distribution models—tools for a description of the heterogeneity of the magmatic field as reflected in the geochemistry of a growing crystal. *Acta Geol Pol* 62:129–141
- Stengel MO (1977) Normalschwingungen von Alkalifeldspaten. *Zeitschrift fuer Kristallographie* 146:1–18
- Svahnberg H, Piazzolo S (2013) Interaction of chemical and physical processes during deformation at fluid-present conditions: a case

- study from an anorthosite–leucogabbro deformed at amphibolite facies conditions. *Contrib Mineral Petrol* 165:543–562
- Tsurumi J, Hosonuma H, Kanagawa K (2003) Strain localization due to a positive feedback of deformation and myrmekite—forming reaction in granite and aplite mylonites along Hatagawa shear zone of NE Japan. *J Struct Geol* 25:557–574
- Vėjelytė I (2011) The Telšiai and Drūkšiai-Polock Deformation Zones: petrography and U/Pb geochronology. Summary of doctoral dissertation. Vilnius University, 50 pp
- Vernon RH (1986) K-feldspar megacrysts in granites—phenocrysts, not porphyroblasts. *Earth-Sci Rev* 23:1–63
- Vernon RH (2004) A practical guide to rock microstructure. Cambridge University Press, Cambridge, p 594
- Vernon RH, Flood RH (1988) Contrasting deformation of S- and I-type granitoids in the Lachlan Fold Belt, eastern Australia. *Tectonophysics* 147:127–143
- Vernon RH, Paterson SR (2008) How late are K-feldspar megacrysts in granites? *Lithos* 104:327–336
- Vernon RH, Williams VA, D’Arcy WF (1983) Grain size reduction and foliation development in a deformed granitoid batholith. *Tectonophysics* 92:123–145
- Yoeli P (1965) Analytical hill shading. *Surv Mapp* 25:573–579
- Zellmer GF, Clavero JE (2006) Using terrace element correlation patterns to decipher a sanidine crystal growth chronology: an example from Taapaca volcano, Central Andes. *J Volcanol Geoth Res* 156:291–301